ETH ZÜRICH

Single-ion addressing using crossed acousto-optic deflectors

Author:
Hendrik TIMME

Supervisors:
Dr. Stephan WELTE
Prof. Jonathan HOME

Trapped Ion Quantum Information
Department of Physics

March 27, 2023

Abstract

Master's Thesis

Single-ion addressing using crossed acousto-optic deflectors

by Hendrik TIMME

This thesis presents the characterization of a single-ion addressing setup for trapped $^{40}Ca^{+}$ ions. Quantum computers have the potential to provide exponential speedup for certain problems, and error correction is crucial to achieving this. Bosonic codes are a promising class of error-correcting codes that can be implemented in trapped ions. To scale up the system to several ions and reach the break-even point in error correction, individual addressing of ions and high Rabi frequencies are essential. In this work, we characterize a single-ion addressing setup using crossed acousto-optic deflectors. We also determine the spot size, operational crosstalk, and beam-pointing error. Our measurements show a horizontal beam waist of less than 2 µm and operational crosstalk of less than 10^{-3} for ions that are 5 µm apart. We develop a model describing fluctuations in the beam position to show that the beam deviates by 13 nm. We also adapt an algorithm to determine the aberrations using an ion to image the laser beam. Our results show that it is a viable system to do fast single-ion addressing with the potential to be used in bosonic encodings in trapped ions.

Acknowledgements

I would like to express my sincere gratitude to several people who have played a significant role in my journey toward completing my studies.

Firstly, I extend my warm thanks to Stephan for being my first contact with the group and for making me feel welcome. Stephan took the initiative to organize lab tours, introduce me to all team members, and answer any questions I had while joining the group. During my thesis, he continued to guide me by showing me how to set up an optical experiment and providing valuable feedback on my ideas.

I am also grateful to Martin for his support throughout my thesis. He patiently explained the ion trapping setup to me and always made time to discuss any obstacles I faced during the experimentation process and analysis of my data.

Moritz's contribution to my work was invaluable. He provided several insightful suggestions for me to explore and was always willing to discuss new approaches I had in mind.

I would like to express my appreciation to all three of them for proofreading my thesis and providing constructive feedback.

I would also like to thank Luca for his camaraderie in B18 at the beginning of my thesis.

The setup that I had the benefit of characterizing from day one was expertly designed, built, and documented by Ralf whose work I relied on during the entirety of my thesis.

Discussions with Alfredo on modeling and measuring the beam-pointing error were immensely helpful. I am grateful to all other TIQI members for creating an enjoyable working environment. It was a pleasure to exchange ideas with each of you.

A special mention goes to Jonathan for his advice and contributions during group meetings. He was furthermore always ready to discuss my research and provide suggestions to improve my work in the lab.

I would like to express my deepest appreciation to my family, particularly my parents, for their unwavering support throughout my studies.

Finally, I am grateful to Lara for being by my side every step of the way during these last few years.

Contents

Abstract **i**

Acknowledgements **ii**

1 Introduction **1**

2 Theory **3**
2.1 Calcium ion as a qubit . . . 3
2.2 Thresholding and quantum projection noise . . . 3
2.3 Ion-light interaction . . . 4
2.3.1 Rabi frequency . . . 5
2.3.2 Solving the Schrödinger equation . . . 6
2.3.3 Lamb-Dicke regime . . . 7
2.3.4 Non-resonant addressing . . . 7
2.4 Laser cooling . . . 8
2.5 Gaussian beam . . . 9
2.6 Acousto-optics . . . 10

3 Characterization of addressing setup **12**
3.1 Overview over the single-ion addressing setup . . . 12
3.2 Telescope system . . . 12
3.3 Acousto-optical deflectors . . . 14
3.4 Aligning the telescope setup . . . 15
3.5 Polarization dependence of the addressing beam using AODs . . . 17
3.6 Imaging of the beam using the picamera v2 . . . 18
3.7 Characterization of the spot size . . . 20

4 Single-ion addressing **23**
4.1 The ion trapping setup . . . 23
4.2 Individual addressing of ions . . . 25
4.3 Using ions to image the laser beam with high resolution . . . 26
4.4 Extended Nieboer Zernike theory . . . 28
4.5 Beam-pointing error . . . 32
4.6 Characterization of the crosstalk . . . 36

5 Conclusion and outlook **38**

References **40**

A Settings of the camera **45**

B Phase retrieval and simulation using the extended Nieboer-Zernike theory **47**

1 Introduction

Richard Feynman and Yuri Manin introduced the concept of utilizing quantum mechanics for computation [1], [2]. Due to its potential advantages in factoring integers [3], unstructured search [4], and simulating quantum mechanical systems researchers have since dedicated much effort to building a quantum computer. Various architectures for encoding quantum information, referred to as qubits, are being pursued, including superconducting circuits, trapped ions, cold neutral atoms, NV centers, and quantum dots. However, the challenge of dealing with intrinsically noisy qubits persists and remains a major obstacle in realizing a fault-tolerant quantum computer. The no-cloning theorem rules out the most naive method of encoding information, by copying bits of information, fundamentally impossible [5].

To address this issue, several error-correcting codes have been proposed, with the simplest ones being the three-qubit bitflip and phase-flip codes. Shor proposed a design that combines both codes to correct arbitrary single qubit errors [6]. Another approach to utilizing ancillary qubits is surface codes, defined on a 2D lattice of qubits.

Fundamentally different are bosonic codes. Instead of using 2-level systems as ancillary qubits, they use a larger (theoretically infinite, in practice truncated) Hilbert space to encode information. One example of a bosonic code is the GKP-code [7]. Using trapped ions as an architecture the ion's motional mode is used to encode information [8]. Although encoding information in GKP states, error-correcting it [9], and performing arbitrary gates have been experimentally demonstrated, two significant challenges must still be overcome: the break-even point for fault-tolerant encoding and the demonstration of two-qubit gates for GKP states. Following on from the work [10] it has been shown that we can do state-dependent forces necessary for implementing GKP codes at high Rabi frequencies.

In this thesis, we present the work towards a single-ion addressing setup. By focusing the laser beam driving the qubit transition tightly we can tackle both problems at the same time: A small spot size means that the electric field amplitude, which is proportional to the Rabi frequency, will be high. It also allows individual addressing of ions which is a necessary ingredient to perform a two-qubit gate.

We will start the thesis in Chapter 2 by presenting the necessary theoretical frameworks to understand the individual addressing of ions. We will show how a Calcium ion can be used as a qubit. We then derive the interaction between ions and light focusing on aspects important for understanding the addressing of the optical transition used as a qubit. We describe a Gaussian beam and how it propagates. We then show how light and acoustic waves interact in a crystal to understand the component used to steer the beam, an acousto-optic deflector.

Chapter 3 will present the work done in aligning and characterizing the experimental setup. We will start by describing the experimental setup and the design choices while building it. We rely heavily on Ralph Berner's work [11] who designed and build the addressing setup. We then show measurements of the polarization depending on the radio frequency applied to the acousto-optic deflectors and measure the beam waist of the focused beam to evaluate whether it can be used to address ions individually.

Chapter 4 will present the work done in situ. We will briefly present the experimental setup and then describe the procedure on how to address ions. We show how we can image the laser beam

and then use the same technique to calculate a ratio between frequencies applied to the steering AODs deflectors and the distance that will move the focused spot in the trap. We also show how the imaging technique could be used to characterize aberrations in the system. We develop a model to measure the beam-pointing error and use it to get an upper bound on the movement of the beam. Finally, we measure the crosstalk between individually addressed ions.

2 Theory

We will start with a description of the level scheme of $^{40}Ca^+$ Calcium, and the necessary lasers to address the relevant transitions. We then describe the optical readout. We describe a two-level system interacting with an oscillating electric field, going into detail to describe the Rabi frequencies for quadrupole-allowed transitions. We then give a short introduction to Gaussian beams and acousto-optic effects.

2.1 Calcium ion as a qubit

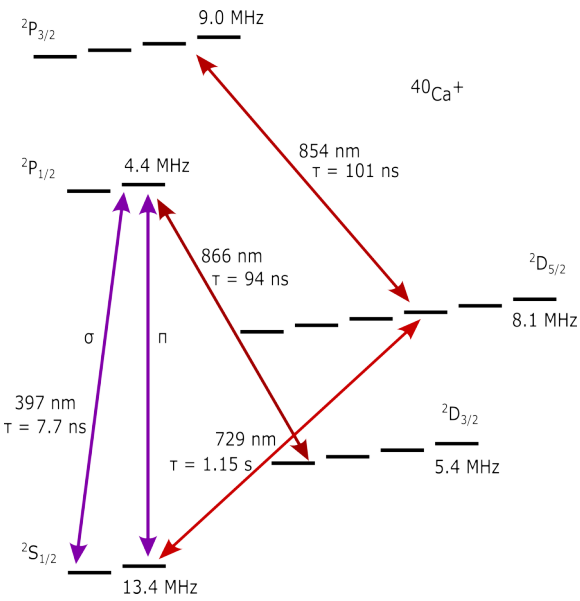

FIGURE 2.1: Level scheme for $^{40}Ca^+$ at 4.8 G calculated using the spectrum obtained, see figure 4.6. Zeeman splitting is given in $\frac{\omega}{2\pi}$. Calculated using table 3.2 in [12].

The addressing system will focus the laser beam driving the optical qubit transition of a Calcium $^{40}Ca^+$ ion. An energy level scheme with relevant transition and lasers that we use to drive transitions in the ion can be seen in figure 2.1. A $^{40}Ca^+$ ion is singly charged with a single valence electron. We use spectroscopic notation $n^{2S+1}L_J$ to denote the energy levels where n is the principal quantum number, S the spin angular momentum, L the orbital angular momentum, J the total angular momentum and m_J its projection onto the quantization axis. In a Calcium ion, it is possible to choose Zeeman-sublevels as a qubit system or choose an optical transition. Here we will use an optical transition. Because the $D_{5/2} \leftrightarrow S_{1/2}$ transition is dipole forbidden, the electron will couple to the gradient of the electric field as a quadrupole transition. This makes the coupling by a factor $(ka_0)^2)$ weaker. It has a lifetime of $\tau \sim 1.15$s and thus a linewidth of $\Gamma \approx 2\pi \times 138$mHz [13]. This makes it a good candidate for the qubit states $|0\rangle$ and $|1\rangle$. Transitions are allowed for $\Delta L = 2$ and $\Delta m_L = 0, \pm 1, \pm 2$ depending on the angle of the polarization and the magnetic field, see 2.3.1.

To read out the electronic state of the ion, we use the $P_{1/2} \leftrightarrow S_{1/2}$ transition which will produce fluorescence while driving the laser only when the qubit is in the $|0\rangle$ state. Whenever we drive the $P_{1/2} \leftrightarrow S_{1/2}$ transition the state might also decay into the $D_{3/2}$ manifold. During the readout we also strongly drive the $P_{1/2} \leftrightarrow D_{3/2}$ transition with a repumper that pumps the $P_{1/2} \leftrightarrow D_{3/2}$ with a wavelength of 866nm. In the same way, we might want to drive the $P_{3/2} \leftrightarrow D_{5/2}$ so that the state will decay into the $S_{1/2}$. See figure 4.5 for a typical experimental sequence using all lasers depicted.

2.2 Thresholding and quantum projection noise

Here we follow the discussion in [14]. After collecting the fluorescence, we use histogram thresholding to determine the population in each of the qubit states. See [15] for a reference going into detail.

We measure the ion in states $|1\rangle$ and $|0\rangle$, as bright and dark states, respectively. During the detection time τ, we measure a histogram $H(n)$ of photon counts. For one ion, we will find the sum of two Poissonian distributions for the state being bright or dark $H(n) = S(n) + D(n)$, where

$$D(n) = \frac{\mu_D^n e^{-\mu_D}}{n!} \tag{2.1}$$

$$S(n) = \frac{\mu_B^n e^{-\mu_B}}{n!}. \tag{2.2}$$

Here, μ_D and μ_B are the mean numbers of photons for the dark and bright states. The best threshold to distinguish the two distributions is [15]:

$$n_{\text{thresh}} = \frac{\mu_B - \mu_D}{\ln(\mu_B/\mu_D)} \tag{2.3}$$

We conclude that the final state is $|1\rangle$ if the number of photon counts at the photomultiplier tube is larger than n_{thresh}, and $|0\rangle$ if it is smaller.

We then repeat the experiment N times. The thresholding technique allows us to convert photon counts to populations $p(0) = p_D$ and $p(1) = p_S$ which are probabilities that the qubit is in state $|0\rangle$ or $|1\rangle$. If after N experiments n trials returned the result $|0\rangle$, we estimate the probability $P(0) = \frac{n}{N}$. The uncertainty is the quantum projection noise [16]:

$$\sigma_{P(0)} = \sqrt{\frac{P(0)(1-P(0))}{N}}. \tag{2.4}$$

This underestimates the uncertainty in two cases when $p(0) \approx 0$ or $p(0) \approx 1$. We can solve this by applying Laplace's succession rule and imposing a minimum uncertainty of [17]

$$\sigma_{p(0)} = \max\left\{\sqrt{\frac{p(0)(1-p(0))}{N}}, \frac{1}{N+2}\right\}. \tag{2.5}$$

We will use this uncertainty for any measurement involving thresholding in chapter 4.

It is also possible to detect the states of more than one ion using thresholding of photon count distributions. For two ions, we fit the detection histogram with three Poisson peaks with means μ_{DD}, μ_{DB}, μ_{BB} and then find two thresholds that distinguish the three distributions. We then obtain the probabilities $p00)$, $p(01+10)$, and $p(11)$, where $p(01+10)$ is the sum of the populations of $|01\rangle$ and $|10\rangle$. Although this works for two ion experiments, it is not possible to scale this approach to a larger number of ions because the variance of a Poisson distribution with mean n is $\sqrt{n}$. For N ions, the variances $\sqrt{N \times \mu_B}$ for N bright ions will be larger than the distance between the peaks of the distribution, making readout impossible. Even for the case of two ion experiments, the larger variances are already a leading source of error for readout [14].

2.3 Ion-light interaction

We want to describe the interaction of a trapped ion driven by a coherent light source. We will follow the treatment in [18]. The Hamiltonian describing the ion interacting with a coherent light source is

$$H = H_a + H_m + H_{\text{int}} \tag{2.6}$$

where H_a describes the internal states, H_m describes the motion of the atom, and H_{int} is the interaction between the ion and the electromagnetic field.

We start by looking at the atomic part H_a. We want to restrict the Hamiltonian to a two-level. We will assume that $|g\rangle$ and $|e\rangle$ are the relevant parts of the two-level quantum system with other parts

far off-resonance from the addressing light. For a two-level system, we find

$$H_e = \frac{\hbar\omega_0}{2}\left(|e\rangle\langle e| - |g\rangle\langle g|\right) = \frac{\hbar\omega_0}{2}\sigma_z \tag{2.7}$$

where $\sigma_z = |e\rangle\langle e| - |g\rangle\langle g|$. Because the ions are trapped in a linear Paul trap their motion is described by a harmonic oscillator

$$H_m = \left(a^\dagger a + \frac{1}{2}\right)\hbar\omega_m, \tag{2.8}$$

where ω_m is the frequency of the oscillator motion and $a^\dagger$ and a are the creation and annihilation operators. We will consider only one motional mode, the others will behave analogously.

To find the interaction Hamiltonian we can go to the dipole approximation, the case for the quadrupole-allowed transitions is also covered in this way by considering the corresponding Rabi frequency for quadrupole transitions. The dipole interacts with the electric field along z

$$\mathbf{E} = E_0\hat{x}\cos\left(\omega_L t - kz\right), \tag{2.9}$$

where E_0 is the electric field amplitude and ω_L the frequency of the light. The Hamiltonian describing the interaction in the dipole approximation is then

$$H_{\text{int}} = \frac{\hbar\Omega}{2}\left(\sigma_+ + \sigma_-\right)\left(e^{i(\omega_L t - kz)} + e^{-i(\omega_L t - kz)}\right) \tag{2.10}$$

where we have expressed $\hat{x}\cdot\mathbf{D}$ as

$$\hat{x}\cdot\mathbf{D} \equiv \langle e|\,\hat{x}\cdot\mathbf{D}|\,|g\rangle\left(|e\rangle\langle g| + |\,|g\rangle\langle e|\right) \tag{2.11}$$

$$= \Omega\left(\sigma_+ + \sigma_-\right) \tag{2.12}$$

with $\sigma_+ = |e\rangle\langle g|$ and $\sigma_- = |g\rangle\langle e|$ and the Rabi frequency $\Omega = -\frac{E_0}{\hbar}\langle \mathrm{e}|\hat{x}\cdot\mathbf{D}|\mathrm{g}\rangle$.

2.3.1 Rabi frequency

The Rabi frequency describes the frequency of the oscillations between the ground and excited states. The matrix elements can be expressed as a function of the decay rate. See [12] for the full derivation. For the dipole transition, they are

$$\Omega^{\text{DP}} = \frac{eE_0}{\hbar}\left(\frac{3\left(2j_e+1\right)\Gamma^{\text{DP}}_{e\bar{g}}}{4c\alpha k^3}\right)^{1/2}\left|\sum_m \begin{pmatrix} j_e & 1 & j_g \\ -m_e & m & m_g \end{pmatrix} \boldsymbol{c}^{(m)}\cdot\epsilon\right| \tag{2.13}$$

For a quadrupole-allowed transition, we can follow the same derivation with the Rabi frequency:

$$\Omega^{\text{QP}} = \frac{eE_0}{\hbar}\left(\frac{15\left(2j_e+1\right)\Gamma^{\text{QP}}_{e\bar{g}}}{4c\alpha k^3}\right)^{1/2}\left|\sum_m \begin{pmatrix} j_e & 2 & j_g \\ -m_e & m & m_g \end{pmatrix} \sum_{i,j} c^{(m)}_{ij}\kappa_i\epsilon_j\right|. \tag{2.14}$$

where the j and m components are angular-momentum quantum numbers, $\Gamma^{\text{DP/QP}}_{e\bar{g}}$ the decay rate, and

$$\alpha = \frac{e^2}{4\pi\epsilon_0\hbar c} \tag{2.15}$$

the fine structure constant. The final term gives the selection rule based on the Wigner 3-j symbols, representing a number.

Following Appendix A.1 in [19] we can simplify the expression. Relating the Wigner 3-j symbols

m	$\pm 1/2$	$\pm 1/2$	$\pm 1/2$	$\pm 1/2$	$\pm 1/2$
m'	$\pm 5/2$	$\pm 3/2$	$\pm 1/2$	$\mp 1/2$	$\mp 3/2$
$\Lambda(m, m')$	1	$\sqrt{4/5}$	$\sqrt{3/5}$	$\sqrt{2/5}$	$\sqrt{1/5}$

TABLE 2.1: Relevant specific Clebsch-Gordan coefficients, taken from Appendix A.1 in [19].

to the Clebsch-Gordan coefficients and using their properties we find

$$\Omega = \frac{eE_0}{2\hbar}\sqrt{\frac{15\Gamma^{\mathrm{QP}}_{e\tilde{g}}}{c\alpha k^3}}\Lambda(m, m')\, g^{(\Delta m)}(\phi, \gamma) \tag{2.16}$$

with $g^{(\Delta m)}(\phi, \gamma)$ being a geometrical factor and $\Lambda(m, m')$ given in table 2.1. The geometrical factors are dependent on the angle between the magnetic field and the laser beam ϕ and between the magnetic field and the polarization γ. They are:

$$\begin{aligned} g^{(0)} &= \frac{1}{2}|\cos\gamma\sin(2\phi)| \\ g^{(\pm 1)} &= \frac{1}{\sqrt{6}}|\cos\gamma\cos(2\phi) + i\sin\gamma\cos\phi| \\ g^{(\pm 2)} &= \frac{1}{\sqrt{6}}\left|\frac{1}{2}\cos\gamma\sin(2\phi) + i\sin\gamma\sin\phi\right|. \end{aligned} \tag{2.17}$$

We can maximize the Rabi frequency by addressing the $S_{\{1/2,1/2\}} \leftrightarrow D_{\{5/2,5/2\}}$ transition and choosing $\phi = \gamma = \frac{\pi}{2}$, so that $\Lambda(m, m') = 1$ and $g^{(\Delta m)}(\phi, \gamma) = \frac{1}{\sqrt{6}}$. The maximal Rabi frequency on the $S_{\{1/2\}} \leftrightarrow D_{\{5/2\}}$ we can reach given an electric field E is then

$$\Omega = \frac{eE}{\hbar}\sqrt{\frac{5\lambda^3\Gamma^{\mathrm{QP}}_{e\tilde{g}}}{64\pi^3 c\alpha_0}} \tag{2.18}$$

2.3.2 Solving the Schrödinger equation

We now go to the interaction picture by a unitary operation. We define $U = e^{-iH_0 t/\hbar}$ with $H_0 = H_e + H_m$ and can transform the interacting part of the Hamiltonian using

$$\tilde{H}_{int} = U^\dagger H_{\mathrm{int}}\, U \tag{2.19}$$

We find for the transformed Hamiltonian $\tilde{H}_{int}$

$$\tilde{H}_{int} = \frac{\hbar\Omega}{2}\left(\sigma_+ e^{i\omega_0 t} + \sigma_- e^{-i\omega_0 t}\right)\left(e^{i\omega_L t}e^{iH_m t/\hbar}e^{-ikz}e^{-iH_m t/\hbar} + e^{-i\omega_L t}e^{iH_m t/\hbar}e^{ikz}e^{-iH_m t/\hbar}\right). \tag{2.20}$$

We can simplify the expression further by the rotating-wave approximation. It is a good approximation for an atom that is weakly coupled to the electric field $\Omega \ll \omega_0$ with a laser frequency that is tuned near resonance $|\omega_L - \omega_0| \ll \omega_0$. The terms oscillating fast can then be averaged over and we find

$$\tilde{H}_{int} = \frac{\hbar\Omega_0}{2}\left(\sigma_+ e^{-i\delta t}e^{i\eta\left(\tilde{a}^\dagger + \tilde{a}\right)} + \sigma_- e^{i\delta t}e^{-i\eta\left(\tilde{a}^\dagger + \tilde{a}\right)}\right), \tag{2.21}$$

where $\delta = \omega_L - \omega_0$ is the detuning of the laser and $\tilde{a} = ae^{i\omega_z t}$ is the annihilation operator in the interaction picture.

$\eta = k\sqrt{\hbar/2m\omega_z}$ is the Lamb-Dicke parameter, which occurs after rewriting the electric field in terms of creation and annihilation operators. It determines the coupling strength between the atomic and

motional states of the ion. Going into the interaction picture we can write the state vector as

$$|\psi_{\text{int}}\rangle = \sum_{n=0}^{\infty} C_n(t)\,|g,n\rangle + D_n(t)\,|e,n\rangle\,, \tag{2.22}$$

where $C_n(t)$ and $D_n(t)$ are the time-dependent coefficients of the ground- and excited states and $|n\rangle$ denotes the motional mode. We can then write the Schödinger equation as

$$\begin{bmatrix} D_{n'}(t) \\ C_n(t) \end{bmatrix} = \mathcal{M}_{n',n} \begin{bmatrix} D_{n'}(0) \\ C_n(0) \end{bmatrix}, \tag{2.23}$$

and solve it analytically

$$\mathcal{M}_{n',n} = \begin{bmatrix} e^{-\frac{i\Delta t}{2}}\left\{\cos\left(\frac{\tilde{\Omega}t}{2}\right) + i\frac{\Delta}{\tilde{\Omega}}\sin\left(\frac{\tilde{\Omega}t}{2}\right)\right\} & -i\frac{\Omega_{n',n}}{\tilde{\Omega}}e^{i\left(|n'-n|\frac{\pi}{2}-\frac{\Delta t}{2}\right)}\sin\left(\frac{\tilde{\Omega}t}{2}\right) \\ -i\frac{\Omega_{n',n}}{\tilde{\Omega}}e^{-i\left(|n'-n|\frac{\pi}{2}-\frac{\Delta t}{2}\right)}\sin\left(\frac{\tilde{\Omega}t}{2}\right) & e^{\frac{i\Delta t}{2}}\left\{\cos\left(\frac{\tilde{\Omega}t}{2}\right) - i\frac{\Delta}{\tilde{\Omega}}\sin\left(\frac{\tilde{\Omega}t}{2}\right)\right\}, \end{bmatrix} \tag{2.24}$$

where $\Delta = \omega_L - \omega_0 - l\omega_z$ is the detuning from the lth sideband meaning $l = n' - n$. $\Omega_{n',n} = \Omega_0 \left|\left\langle n' \left| e^{i\eta\left(a+a^\dagger\right)} \right| n \right\rangle\right|$ is the Rabi frequency of the lth sideband. By detuning the laser resonantly with the respective sideband we can couple to the motional states of the ion. $\tilde{\Omega} = \sqrt{\Omega_{n',n}^2 + \Delta^2}$ denotes the Rabi frequency detuned to the transition of a particular sideband.

2.3.3 Lamb-Dicke regime

We can now go to the Lamb-Dicke Regime which is valid when the size of the wave function of the ion is small compared to the wavelength of the light. Then terms higher order in η are small and we expand the Hamiltonian in first order

$$\tilde{H}_{\text{int}} \approx \frac{\hbar\Omega_0}{2}\left(\sigma_+ e^{-i\delta t}\left[1 + i\eta\left(\tilde{a}^\dagger + \tilde{a}\right)\right] + \text{H.c.}\right), \tag{2.25}$$

where H.c. denotes a second term which is the hermitian conjugate of the first term in the brackets. The Rabi frequencies of the carrier, red- and blue sideband in the first order are then

$$\begin{aligned} \Omega_{carrier} &= \left(1 - \eta^2\left(n + \frac{1}{2}\right)\right)\Omega_0, \\ \Omega_{rsb} &= \sqrt{n}\,\eta\,\Omega_0, \\ \Omega_{bsb} &= \sqrt{n+1}\,\eta\,\Omega_0, \end{aligned} \tag{2.26}$$

We can see that for a small Lamb-Dicke parameter, we need large Ω_0 to drive fast sideband transitions. We can achieve that by focusing the addressing beam tightly, see section 2.5 because Ω_0 is proportional to the electric field.

2.3.4 Non-resonant addressing

If we address any transition off-resonantly the states will be shifted by the AC-Stark effect. We write the Hamiltonian as

$$\tilde{H}_{\text{Stark}} = \frac{\hbar\delta}{2}\sigma_z + \frac{\hbar\Omega_0}{2}\left(\sigma_+ + \sigma_-\right), \tag{2.27}$$

where $\delta = \omega_L - \omega_0$ is the detuning. By going into the frame rotating with the frequency of light we can eliminate the time dependence. We then find the eigenvalues of the system

$$\begin{aligned} E_{\text{Stark}} &= \pm\sqrt{\frac{\hbar^2\Omega_0^2}{4} + \frac{\hbar^2\delta^2}{4}} \\ &\approx \pm\left[\frac{\hbar\delta}{2} + \frac{\hbar\Omega_0^2}{4\delta}\right] \text{ for } \delta \gg \Omega_0. \end{aligned} \tag{2.28}$$

If $\delta \gg \Omega_0$ the light shifts the dressed states additionally by $\frac{\Omega_0^2}{2\delta}$ [18]. When we drive the carrier transition on resonance the energy levels will split by $\pm\frac{\Omega_0}{2}$. This is called the Autler-Townes effect [20].

This shift must be taken into account whenever we want to drive any transition. Because it is dependent on Ω_0 this effect is generally larger for a dipole than for a quadrupole-allowed transition and larger for the carrier than for sideband transitions. In our case we will reach Rabi frequencies Ω_0 larger than 10MHz on the carrier, so the effect is also significant for sideband transitions.

$$P_e(t) = \frac{\Omega_0^2}{\Omega_0^2 + \Delta^2}\sin^2\left(\frac{\sqrt{\Omega_0^2 + \Delta^2}}{2}t\right). \tag{2.29}$$

If the detuning is zero we record Rabi oscillations on the Carrier

$$p_g(t) = \cos^2(\Omega_0 t/2) \tag{2.30}$$

$$= \frac{1}{2} + \frac{1}{2}\cos(\Omega_0 t) \tag{2.31}$$

2.4 Laser cooling

Laser cooling has first been experimentally observed in 1978 [21]. Fundamentally laser cooling relies on momentum exchange between the ion and photons. Most experiments performed on ions in this thesis have utilized two laser cooling techniques, Doppler cooling, and EIT cooling. An ion at rest, continuously driven by a laser beam, experiences the radiation pressure force

$$\boldsymbol{F}(\delta) = \Gamma\hbar\boldsymbol{k}\frac{\Omega^2}{\Gamma^2 + 2\Omega^2 + 4\delta^2}. \tag{2.32}$$

An ion moving at velocity $\boldsymbol{v}$ experiences the laser frequency detuned as $\delta_{\text{D}} = -\boldsymbol{k}\cdot\boldsymbol{v}$. For $\delta < 0$ the ion scatter more photons towards the direction of the laser and is thus losing momentum along this direction. On the other hand, the ion is also heating up due to random absorption and emission. This gives us a theoretical limit for the temperature of the ion at which the effects cancel out:

$$T_{min} = \frac{\hbar\Gamma}{2k_B} \tag{2.33}$$

After Doppler cooling the ion, we can further reduce its temperature by applying EIT cooling. We use a three-level Λ-system and drive one transition strongly with a $\sigma^{+/-}$-polarized, detuned beam to dress the atom such the AC-Stark shift is equal to the ion's frequency. The polarization depends on the state we want to prepare the qubit in so that we can use the same σ-polarized beam for both EIT cooling and state preparation. This way we can increase the absorption on the red sideband. We can thus theoretically find a cooling limit of

$$\bar{n} = \left(\frac{\Gamma}{4\delta_r}\right)^2, \tag{2.34}$$

where δ_r is the detuning of the laser dressing the atom. See [22] and [23] for a full treatment of EIT cooling and [24] for treatment of Doppler cooling. To cool to the ground state of the oscillator

motion it is possible to drive the red sideband transition to exchange momentum between the ion and light while driving the red sideband. This technique, called sideband cooling, was not used for experiments presented in this thesis.

2.5 Gaussian beam

While plane waves can describe light with wavefront normals pointing in the direction of travel z, their energy is spread out. To describe a laser beam, a better description is made by a wavefront with small angles with respect to the z-direction. A Gaussian beam is such a solution to the paraxial Helmholtz equation. For many lasers, it is a good description of the intensity distribution of the light. The equations characterizing the Gaussian beam are the following. They describe the transverse electromagnetic (TEM) mode. A good overview can be found on the Wikipedia page about the Gaussian beam [25], in chapter 3 of [26] or any other optics book.

$$\tilde{E}(r,z) = E_0 \frac{w_0}{w(z)} \exp\left(\frac{-r^2}{w(z)^2}\right) \exp\left(-i\left(kz + k\frac{r^2}{2R(z)} - \psi(z)\right)\right) \tag{2.35}$$

with

$$\psi(z) = \arctan\frac{z}{z_R} \tag{2.36}$$

the Guoy Phase,

$$R(z) = y\left[1 + \frac{z_R^2}{z_2}\right] \tag{2.37}$$

the radius of curvature of the beam's wavefronts at z and

$$z_R = \frac{\pi\omega_0^2 n}{\lambda} \tag{2.38}$$

the Rayleigh range. It describes the distance away from the focal plane at which the waist is increased by a factor of $\sqrt{2}$.

Its intensity is given by the square of the electric field

$$I(r,z) = \frac{|E(r,z)|^2}{2\eta} = I_0\left(\frac{w_0}{w(z)}\right)^2 \exp\left(\frac{-2r^2}{w(z)^2}\right). \tag{2.39}$$

We can see that the intensity is highest at the focus plane. The beam width can be derived from the Helmholtz equation. It is

$$w(z) = w_0\sqrt{1 + \left(\frac{z}{z_\mathrm{R}}\right)^2}. \tag{2.40}$$

It is minimized at the focal plane, where it is

$$w_0 = \sqrt{\frac{\lambda z_0}{\pi}} \tag{2.41}$$

λ being the wavelength of the light. A Gaussian beam that is collimated, with Rayleigh range $z_0 \to \infty$, will be focused by a thin lens. The waist of the outgoing beam w_0' is

$$w_0' = \frac{\lambda f}{\pi w_0}, \tag{2.42}$$

where f is the focal length of the lens. For a given lens we can thus decrease the waist size of the focused beam by increasing the waist of the incoming beam.

2.6 Acousto-optics

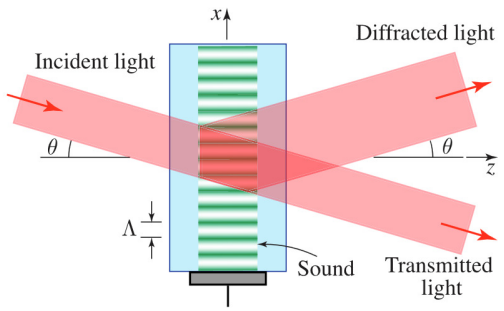

FIGURE 2.2: Scheme of Bragg diffraction: Incident light diffracts on an optical plane wave with wavelength Λ when its angle of incidence θ satisfies the Bragg condition. Figure taken from [26]

AODs are acousto-optic devices, which diffract light on sound waves in a crystal. Brillouin first predicted this in 1922 [27]. Their operation is characterized by Bragg scattering which was experimentally discovered in 1932 [28]. The energy and momentum of the photons of the incoming laser beam and the phonons of the sound waves produced by the radio frequency signal in the crystal determine the scattering process [29].

A piezo-electric transducer is bonded to a crystal. In the device, we will use it, is TeO_2. By applying radio frequency to it, the piezo element will generate an acoustic wave that travels through the crystal. We will give a short derivation following chapter 20 in [26]:

We model the light as an optical plane wave at frequency ν and wavelength $\lambda_o = c_o/\nu$. When propagating through a medium its wavelength is modified by the refractive index $\lambda = \lambda_o/n$. The corresponding wavenumber is $k = n\omega/c_o$, and the wavevector $\mathbf{k}$ lies in the $x - z$ plane. This means it has an angle of θ with the z axis, as shown in figure 2.2. Since the acoustic frequency f is usually in the megahertz regime and the optical frequency ν in the terahertz regime, we can use the adiabatic approach to describe the light-sound interaction. Assuming that the crystal is rectangular, the acoustic waves created by the piezo element will change the refractive index n in a static cosine pattern:

$$n(x,t) = n - \Delta n_0 \cos\left(\Omega_s t - qx\right), \tag{2.43}$$

where Δn_0 is the amplitude of the perturbation, Ω the frequency and q the wave number. We can then calculate the reflectance by assuming it is approximately constant in a thin layer of the crystal (compared to the wavelength of the acoustic wave) and integrating it over slices of the crystal. The resulting reflectance r has two contributions $r = r_+ + r_-$ with

$$r_\pm = \pm i r_0 \operatorname{sinc}\left[(2k\sin(\theta) \mp q)\frac{L}{2\pi}\right] e^{\pm i\Omega_s t}, \tag{2.44}$$

where L is the overall length of the crystal and $r_\pm$ being plus- and minus first-order diffraction. At

$$2k\sin\theta = \pm q \tag{2.45}$$

the Bragg condition is met and we maximize the diffraction efficiency. For large crystals the peak around the maxima is narrow. That means it is useful to have the option to optimize the angle of the light between the incoming light and the acousto-optic device, which informed the design process of the addressing setup. We can define the Bragg angle $\theta_B = \sin^{-1} q/2k$ and rewrite the Bragg condition:

$$\sin\theta_B = \frac{\lambda}{2\Lambda}, \tag{2.46}$$

where Λ is the wavelength of the acoustic wave. We can also see that when the Bragg condition is met that the light will acquire an additional phase. Written using wavevectors we can write the Bragg condition also as conservation of momentum:

$$\mathbf{k_r} = \mathbf{k} + \mathbf{q}, \tag{2.47}$$

where $\mathbf{k_r}$ is the wavevector of the reflected light wave. That means the frequency of light will be shifted by the frequency of the soundwave. Depending on the sign of the shift we call the interaction

plus or minus first-order diffraction.

While until now, we have assumed that the crystal is isotropic, meaning that the sound wave travels longitudinally, the actual crystal in the AOD is anisotropic. That means that the polarization of the light will not stay constant so the refractive indexes will be different for the incoming and outgoing beams. That means the acoustic wave will travel in a shear mode [30]. This will increase both the acoustic as well as the optical bandwidth.

Two commonly used devices using this effect are acousto-optic modulators (AOMs) and acousto-optic deflectors (AODs). The difference between an acousto-optic modulator and a deflector lies in the choice of crystal and the speed of sound in it. While for the AOD we use, the material-acoustic mode-velocity is $650\frac{\mathrm{m}}{\mathrm{s}}$ [31] a comparable AOM has a material-acoustic mode-velocity of $4200\frac{\mathrm{m}}{\mathrm{s}}$ [32]. Thus AOMs have a faster rise time, while AODs have a wider diffraction angle, making AOMs well-designed to modulate the frequency of light and shape pulses, while AODs are better at deflecting light over a wider angle for the individual addressing of atoms over a larger area or use as an optical tweezer.

3 Characterization of addressing setup

3.1 Overview over the single-ion addressing setup

In this section, we will describe the optical setup. It was designed for the following goals:

- a small spot size (smaller than 3 µm beam-waist) to minimize crosstalk and allow single-ion addressing. Given enough input power, this also allows driving of fast Rabi oscillations even on motional sidebands.
- beam spot must be controllable along horizontal direction without changing in frequency and intensity, the addressing range must be large compared to the spot size
- possibility to produce two spots at the same time.
- allows for imaging of the ions along the same axis as the incoming qubit laser.

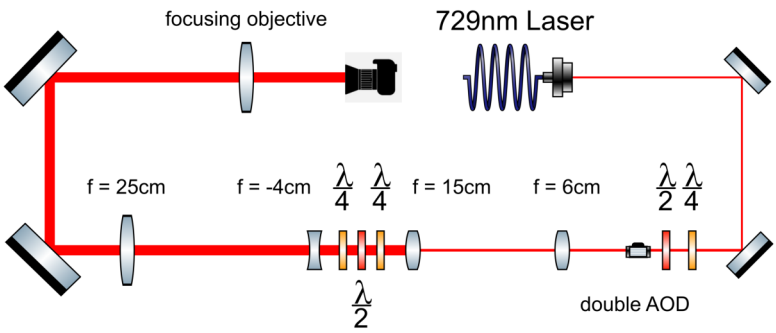

FIGURE 3.1: Schematic drawing of the setup for characterizing the addressing setup. The light coming from the test laser goes through two wave plates. These change the polarization such that the following acousto-optic deflectors are maximally efficient. The setup and characteristics of the AODs are explained in section 3.3. After being diffracted by the AODs all but one diffraction order is blocked. Directly after, the telescope system magnifies the beam. It is described in 3.2. The second set of wave plates allows the change of polarization after the AODs to address the chosen qubit transition. The final objective focuses the light onto the camera. Later on, we will replace the last mirror with a dichroic mirror and shine the beam on the ions instead of the camera see section 4.1.

Ralf Berner and Stephan Welte designed the telescope system for the addressing light before my arrival. Their work can be found in the internship report by Ralf Berner [11]. Figure 3.1 shows a scheme of the telescope system and figure 3.2 shows a CAD rendering.

3.2 Telescope system

To produce a small spot we use an objective with a high numerical aperture (NA). To minimize the spot size in the focal plane, the telescopes magnify the beam to be as large as possible before the objective. One limiting factor is the amount of clipping of the Gaussian beam on the aperture of the objective. The more we clip the more we see an Airy distribution of the intensity around the focus. Hector Cruz showed that for a ratio of the aperture radius a to the beam waist of ω_0 $\frac{a}{\omega_0} > 2.3$ the intensity ripples of the fundamental Hermite-Gaussian are $< 1\%$ [33]. We will aim for a ratio in this

regime. Another constraint is the addressing range, which is dependent on the angle of the beam at the objective.

In our setup, we use an inverse Galilean telescope behind an inverse Keplerian telescope. This

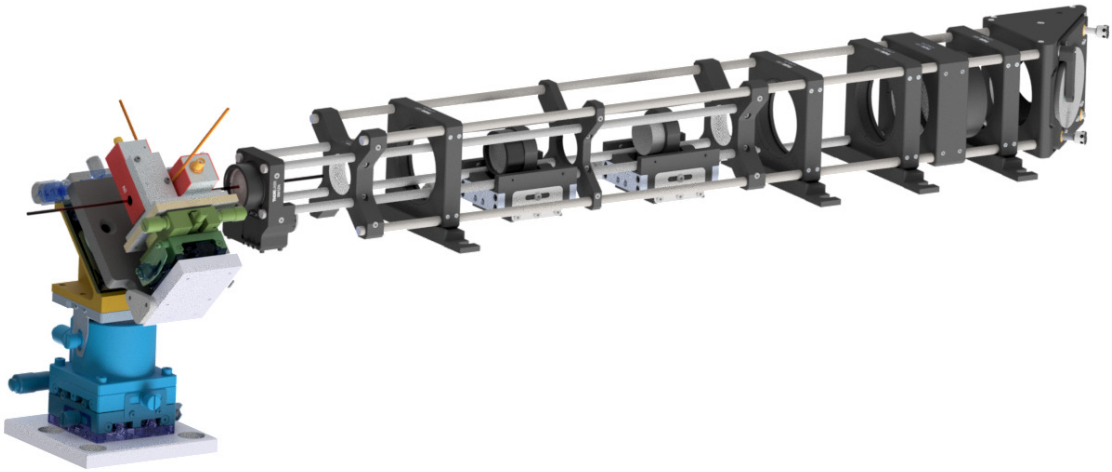

FIGURE 3.2: Render of the two AODs on the top of the 6-axis stage and the telescope setup. On the left, we see the two AODS on a stage that can be translated along all three dimensions and rotated around the axes in red. On the cage system, we see an iris to block all diffraction orders that are not used, followed by the Keplerian and Galileian telescope. At the end of the telescope, a mirror reflects the beam toward the ion trap. Designed and rendered by Ralf Berner.

choice was made with the following constraints in mind:
We assume that we will use a collimator that produces a beam with a waist size of ca. 8mm. For a given telescope the relationship between magnification power M_P and focal lengths f as well as incoming and outgoing angles α is given by:

$$\frac{1}{M_P} = \frac{f_1}{f_2} = \frac{\alpha_{out}}{\alpha_{in}} \tag{3.1}$$

The outgoing angle of the telescope corresponds also to the incoming angle at the objective. This means that the outgoing angle influences the addressing range. To produce a small enough spot size we need a telescope with a magnification power M_P of

$$M_P = 15, \tag{3.2}$$

see [11]. We want to benefit from the wide field of view of a Keplerian telescope while also shortening the system by using a Galileian telescope for the major part of the magnification. In principle, it would be possible to use a 4f system to produce a magnification of $M_P = 15$. If we consider using a lens with focal length $f_1 = 100$mm we can see that the total setup would be longer than 2m and would have to be folded using mirrors. By using a double telescope setup we can fit both telescopes in one cage system. This aids in aligning the telescopes as well as finding a spot on the optical table near the vacuum chamber.

A dichroic mirror makes the imaging and addressing along the same path possible, see figure 4.1 for a scheme of the whole setup. The imaged light of the Calcium ions at 397 nm will go through the mirror to the imaging system. The mirror reflects the addressing light of the 729 nm laser coming from the other side. Using an additional mirror the telescope system is then parallel to the imaging system of the measurement beam. The description of the overall setup will happen in section 4.1.

3.3 Acousto-optical deflectors

To control the position of the beam along the trap axis we use acousto-optic deflectors. We use the model DTSXZ-400-730-020 by AA opto-electronics.

The model DTSXZ-400-730-020 is a combination of two AODs that are aligned with an angle 90° with respect to each other. To align it with respect to the laser beam we mount it on a TSD-605C translation table by Opto Sigma. This way we can translate the AODs along all three dimensions. It has travel distances of ±6.5 mm in x- and y- and ±5 mm in z-direction. It has a load capacity of 15kg. This allows us to mount additional elements on top of it to also align the angle of the AODS.

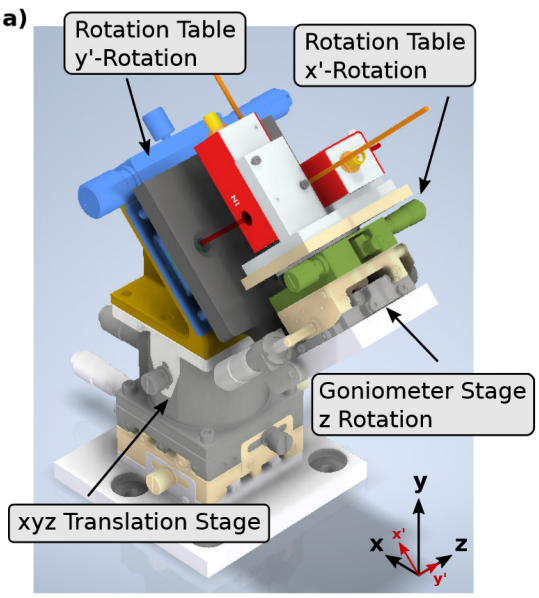

FIGURE 3.3: CAD-model of the AODs on the mount. Design and render by Ralf Berner.

To do that we mount a rotation table for both the x- and y- directions. We choose model RS (KSP-406MR) and model KSP-656M-M6 RT by Opto Sigma for the x- and y-direction respectively. This gives us the ability to rotate the AODs to align the beam such that we maximize the output power by maximizing the diffraction efficiency. Additionally, we mount a Goniometer stage, model GOHT-40A40BMS. This will let us align the horizontal axis along which we plan to diffract the beam with the trap axis.

The acousto-optic deflectors are positioned in a 45° and −45° angle with respect to the vertical plane along the beam path. The idea is to use the first diffraction order of the first AOD and the minus first diffraction order of the second AOD. By applying the same radio frequency to both AODs, the frequency shifts on the light cancel out [34]. If we want to go along the horizontal direction we can apply the same radio frequency to both AODs. This way we can deflect the beam along the trap axis without changing the frequency of the light. A scheme of the diffraction orders is shown in figure 3.5.

The acousto-optic deflectors get supplied with radio frequency. In the first part of this thesis, the signal was generated by an AD9959 board by analog devices. Later on, we switched to DDS channels that are part of the main experimental control system. An introduction to DDS channels can be found in [35]. In short, the steps to generate a signal are:

1. A reference clock provides a signal. According to the tuning register the phase accumulator accumulates phase.
2. Corresponding to the phase the amplitude is retrieved from a look-up table, that is saved on the DDS board
3. A Digital to Analog Converter (DAC) applies the amplitude to an analog signal.
4. The generated signal is filtered to smooth the waveform.

Central Drive Frequency	110MHz
AO Bandwidth	38 MHz
Active Aperture	7.5 mm
Laser Beam Diameter	500µm $< D <$ 6mm
Max RF Power	2W
Material	TeO_2

TABLE 3.1: Excerpt of the test sheet supplied by AA opto-electronic for AOD DTSXZ-400-730-020 [31].

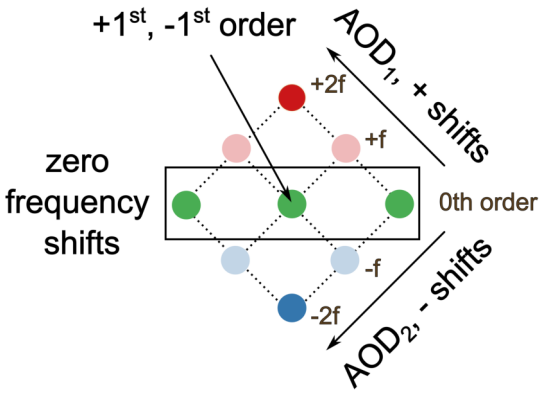

FIGURE 3.5: Scheme of the diffraction pattern created by two crossed AODs. Shown are the positive diffraction orders of the first AOD and the negative orders of the second AOD. We use the first diffraction order of the first AOD and the minus first diffraction order of the second AOD so that the frequency shifts cancel.

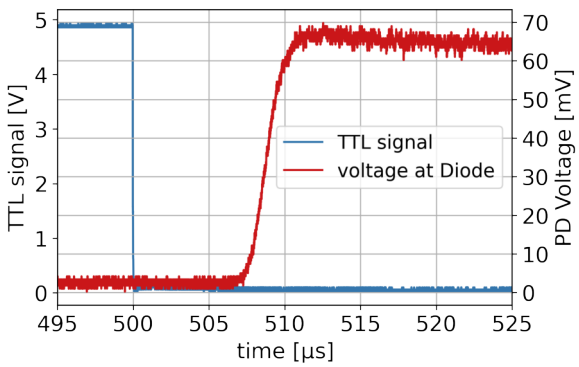

FIGURE 3.4: Rise time measurement of the AOD. There is a delay of ca. 8 µs and the rise time is ca. 4 µs. The voltage at the diode is background corrected. MMt. performed by Ralf Berner. [11]

Table 3.1 summarizes the most important points of the AOD data sheet. They have measured efficiency for the first and minus first order of $> 58\%$ at an applied RF power of 1 W which we have confirmed. The maximally allowed radio frequency power is 2 W. That means we would like to apply radio frequency between 1 and 2 W to the AODs. In both cases, we need to amplify the signal to achieve RF power in this regime. As a pre-amplifier, we use model ZX60-33LNR-S+ by Mini-Circuits which we supply with 5V. As an amplifier, we use model ZHL-2-8-S+ also by Mini-Circuits, which we supply with 24V. To achieve the desired RF power, we use a series of attenuators before the pre-amplifiers. By using 18dB attenuators we can achieve RF power of $30 - 31$dBm as needed.

It is also possible to produce two or more spots at the same time by applying several tones simultaneously. All frequency components arrive at the AODs so that the light diffracts in different directions. This way it is possible to produce a beam that addresses several ions at the same time.

3.4 Aligning the telescope setup

Before beginning to characterize the beam size after the objective we have to align the telescope system: The beam has to go through the AODs such that the efficiency is as high as possible. To reduce

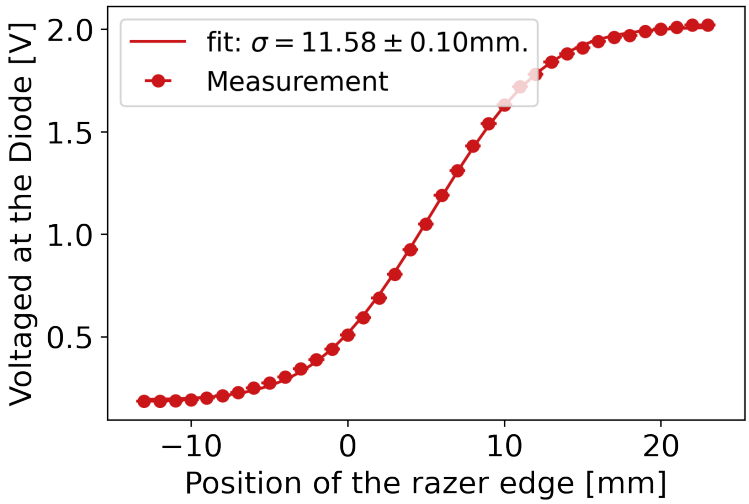

FIGURE 3.6: Razor blade measurement. The scattered points correspond to measured data, while the curve corresponds to the fitted error function. The fitted waist is given in the legend.

aberrations the beam should also propagate centrally through the telescopes. We used anodized aluminum alignment targets by Thorlabs (SCPA 1, and CPA 1) to align the beam along the axis of the optical system. By looking at the beam shape at different points we can avoid clipping that might happen in the mirrors after the telescope.

The goal of the telescope system is to produce a Gaussian beam that is nearly collimated. To that end, we have to exactly set the positions of the telescope lenses with respect to each other. Then we do two measurements of the beam size, spaced apart as far as possible. The beam waist of the measurements should match as closely as possible. By moving the position of the telescope lenses and repeating the measurement we can interpolate the perfect position. This was done behind the first telescope using a Thorlabs beam profiler BC106-VIS. After the second telescope, the beam diameter was too large to use the Thorlabs beam profiler. To measure it, we employed the razor edge method. The method works the following way:

We mount a razor edge on a stage that is translatable in the vertical direction. On top of it, we place a square sheet of black aluminum foil to block the beam. We then place it in the beam path, so that we can move it vertically through the beam. Behind the razor edge, we focus the beam with a lens onto a photodiode at which we read out the voltage. We then move the razor blade through the beam, recording the position of the blade and voltage at the photodiode at each step. The resulting voltage at the diode is proportional to the integral of the intensity of the beam. This is called the error function

$$I(z) = \frac{2}{\sqrt{\pi}} \int_0^z e^{-\left[\frac{\sqrt{2}(z-z_0)}{\sigma}\right]^2} \mathrm{d}z + I_0. \tag{3.3}$$

We can fit this function to our data, by comparing it with equation 2.39. See figure 3.6 for such a measurement, including fit. To ensure that the beam is nearly collimated, we take two measurements: One right after the telescope and one as far away as possible. In this case, they were 80cm apart. Then we change the distance of the telescope lenses with respect to each other and repeat these two measurements. By linearly fitting the fitted radii for either distance of the telescope lens, we can infer the best distance between the telescope lenses, so that the beam is as collimated as possible. This way we collimate the beam approximately up to the precision of the razor edge measurements which is about 0.1µm.

3.5 Polarization dependence of the addressing beam using AODs

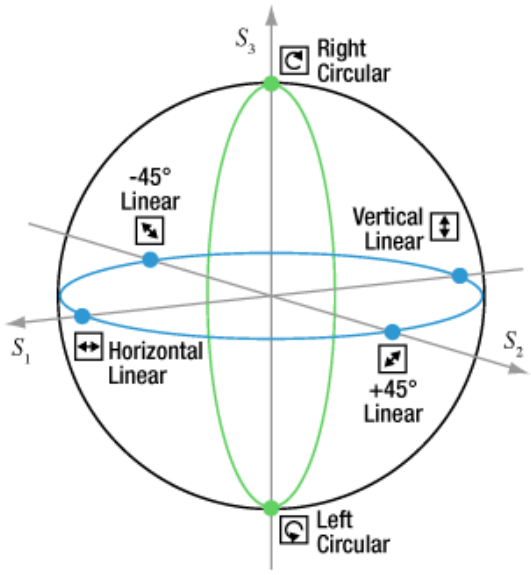

FIGURE 3.7: Poincare sphere as referenced by Thorlabs [36]

To address two ions separately we would like for the intensity and frequency of the light to be constant as we move the laser from one ion to the other. But the atom-light coupling is also dependent on the polarization. To characterize this we measure the effect of different radio frequencies on the polarization of the light. Ideally, the polarization should be independent of the frequency so that the polarization is stable for different positions on the focal plane. In our setup, we have incoming light to the AODs going through a quarter- and a half waveplate to maximize the efficiency of the AODs. Afterward, we want to be able to control the polarization to be optimal for addressing the ion, so we have another set of wave plates in between the two telescopes. In a previous measurement, we saw a slight dependence on the applied radio frequency. However, the measurement was conducted behind the second set of wave plates. One hypothesis that we would like to rule out, is that by applying different radio frequencies to the AODs the light gets deflected and travels at different positions through the wave plates. Because the wave plates are not homogeneous they might change the polarization differently depending on the path the light takes. To rule this out, we took measurements directly after the AODs and after the wave plates and compared them. They are denoted (A) and (B) in figure 3.8. To measure the polarization of the light we used a PAX1000IR1 polarimeter by Thor-

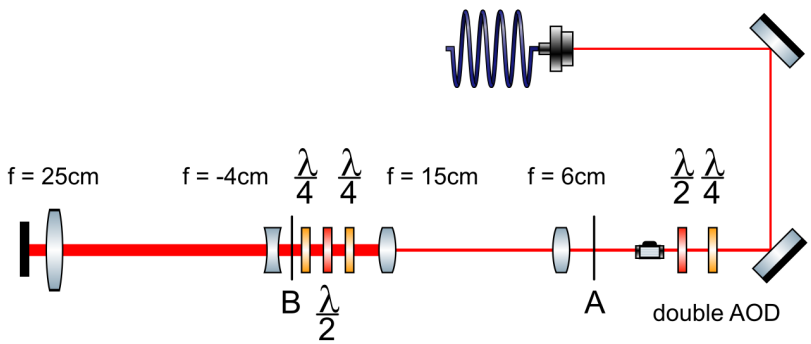

FIGURE 3.8: Part of the single addressing setup with positions A and B showing the positions of the two polarization measurements

labs. We can read out the normalized Stokes vector which represents the coordinates on the Poincare sphere see figure 3.7. Now we can vary the applied RF power and measure the polarization. For each measurement, we use the alignment tool of Thorlabs polarimeter software to position the polarimeter optimally.

The results can be seen in figure 3.9. To better compare the data we do a basis change on the vectors measured directly after the AODs so that the vectors align at the center frequency of 110 MHz. In that way, we can better compare the effect of the wave plates. As can be seen, the change in polarization cannot be explained by the beam traveling through different positions at the wave plates.

Using equation 2.17 we can also quantify the effect on the Rabi frequency. Using the calibration

between the applied radio frequency and the distance along the trap axis in m found in section 4.2 we can give an upper bound on the deviation in the Rabi frequency for different positions at the trap. We can calculate the angle of the polarization using

$$2\psi = \arctan\frac{s_2}{s_1}. \tag{3.4}$$

Using equation 2.17 we find that the Rabi frequency deviates less than 0.01% in a distance of 24µm around the position at the center frequency of 110MHz. In later applications, we might be interested in addressing two ions at different positions in the trap. This effect will probably not be the leading cause of error in the addressing of the different ions. Still, it is possible to calibrate the intensity of the light or the π-time of the qubit gate to cancel this effect. It is also a contribution that could lead to different crosstalk between the two ions which will be characterized in section 4.6.

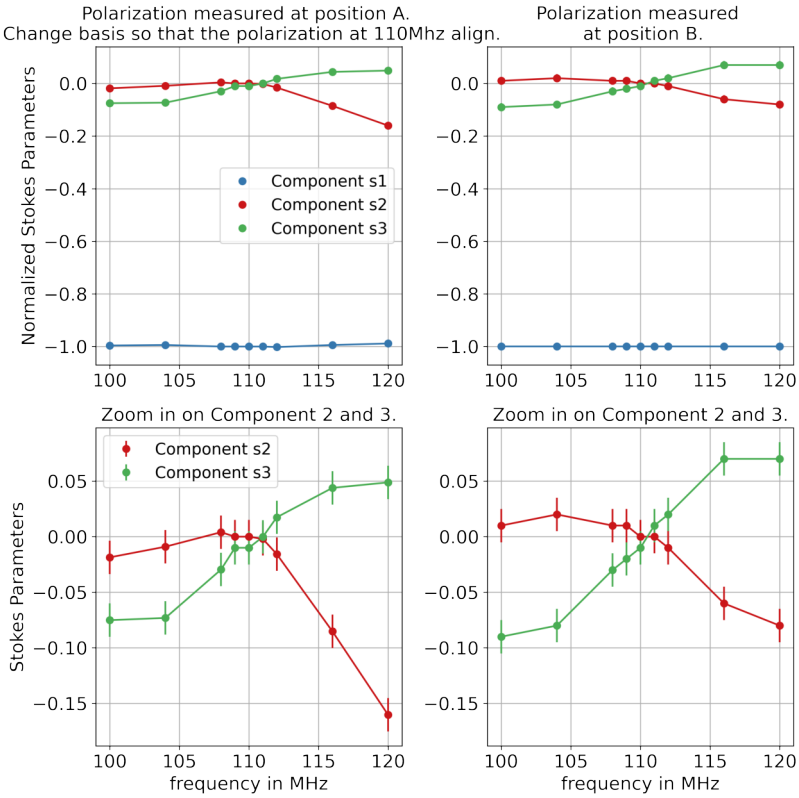

FIGURE 3.9: Polarization dependence on the RF frequency applied to the AODs. Plotted are the normalized Stokes vectors. The left column shows values measured at position A, and the right side values at position B. To better compare both measurements, we changed the basis for the stokes vector on the left side so that the polarization at the center frequency of 110 MHz match.

3.6 Imaging of the beam using the picamera v2

The next step was to measure the beam waist of the focused laser beam after the objective to validate the choice of the telescope setup. To characterize the beam waist of the focused laser beam we planned to use a picamera v2. The main reason is that its pixel size is 1.12 µm × 1.12 µm. Because we expect beam waists in the single micrometer regime, it is not possible to use cameras with larger pixel sizes without using another magnification setup to image the beam. To prepare the camera we removed the lens and the infrared filter with a set of pliers and a knife. Then we built a mount for the camera which we secured to a stage that we can adjust in the $x-$ $y-$ and $z-$direction, see figure A.2. We then positioned it in the beam path, see figure 4.2.

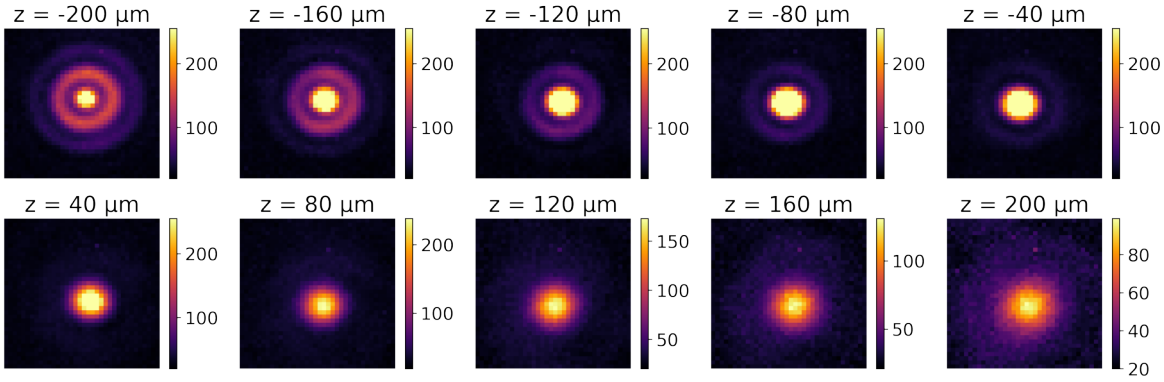

(A) Images were taken with the MPlanApo N 50x objective and FMVU-03MTM firefly camera, the title denotes the distance to the focal plane, with the unit vector pointing along the beam direction.

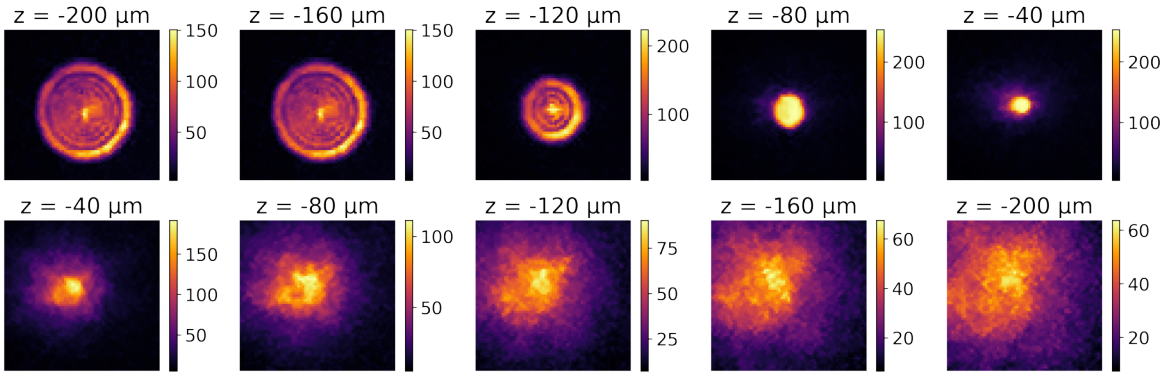

(B) Images were taken with the picamera v2, the title denotes the distance to the focal plane, with the unit vector pointing along the beam direction.

FIGURE 3.11: Comparison of pictures taken with extra imaging objectives vs just a bare sensor. The images are plotted in greyscale with the color denoting the brightness. The images around the focus are overexposed. The scale is also not the same.

Before using the camera to image the laser beam we had to design a setup to reduce the intensity of the laser beam. We used a combination of neutral density filters to reduce the intensity by a constant amount. To also adjust the intensity between different measurement points to account for different intensity amplitudes around the focus plane we included a polarized beam splitter with a wave plate. By changing the angle of the wave plate we could adjust the intensity as needed. To control the camera we use the python package picamera [37]. Then we would adjust the settings as can be seen in listing A.1 in Appendix A and took a series of 100 pictures to average over any fluctuation and reduce the noise. Appendix A also describes the steps taken to calibrate the camera.

Before my arrival, Ralf Berner had already taken photos of the focused beam and noticed rings of intensity appearing in the Gaussian distribution. Back then he used an Olympus MPlanApo N 50x objective to image onto a Point Grey, FMVU-03MTM firefly camera because the pixel size was not big enough to image the beam directly. To investigate, whether the beam itself showed this intensity pattern we compared a series of images around the focus made with the raspberry pi camera and the Olympus MPlanApo N 50x objective, and a firefly camera. The result can be seen in figure 3.11a and 3.11b. We can see that the appearance of the rings is not an artifact of the imaging camera but a property of the focused laser beam. They

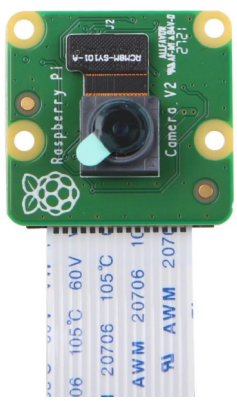

FIGURE 3.10: Picamera v2 [38].

suggest that we are close to the diffraction limit with the rings indicating an airy pattern that we would expect to see for a beam larger than the imaging objective. This intensity pattern was already observed in the thesis of Sylvain de Léséleuc, see figure 2.12 in [39]. They did not make a conclusive state, of whether the imaging system might introduce additional aberrations. We can now say that the effect is also observable with no additional imaging optics.

3.7 Characterization of the spot size

To find the spot size at the focus, we want to fit the function 2.40. To do that we will measure the beam width at several points along the propagation path of the beam. Assuming a perfectly Gaussian mode with no aberrations we would not need to sample very closely around the focus plane and would be able to use a camera with a larger pixel size. As can be seen from earlier measurements in [11] this does not match the actual beam waist around the focal plane very well. We took a series of pictures while moving the camera along the beam propagation. At each point, we would vary the intensity of the laser beam to get an optimal picture and take 100 pictures to average over, as described above. Then we would average over the pictures, and fit a 2-dimensional Gaussian, as can be seen in figure 3.12. Although this process worked well for many pictures, in some cases the aberrations were so strong, that a Gaussian fit does not seem like a good approximation anymore, an example can be seen in figure 3.13. A more thorough investigation of possible aberrations was carried out in section 4.4. In figure 3.15a and 3.15b the fitting of the spot size of the beam along the vertical and horizontal axis

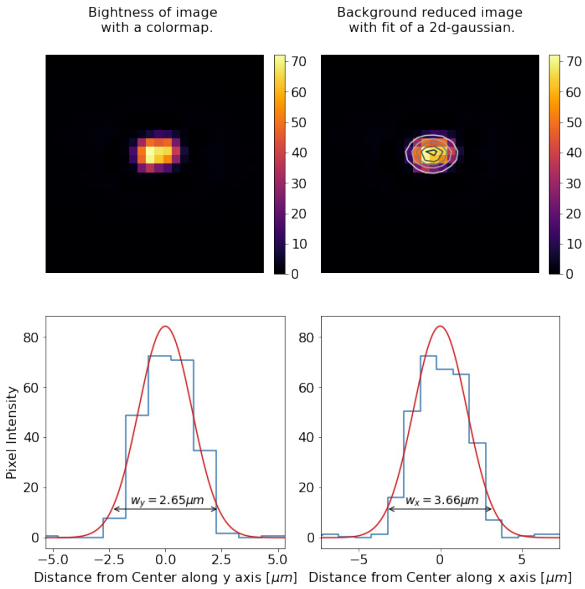

FIGURE 3.12: An example of a Gaussian fit near the focus.

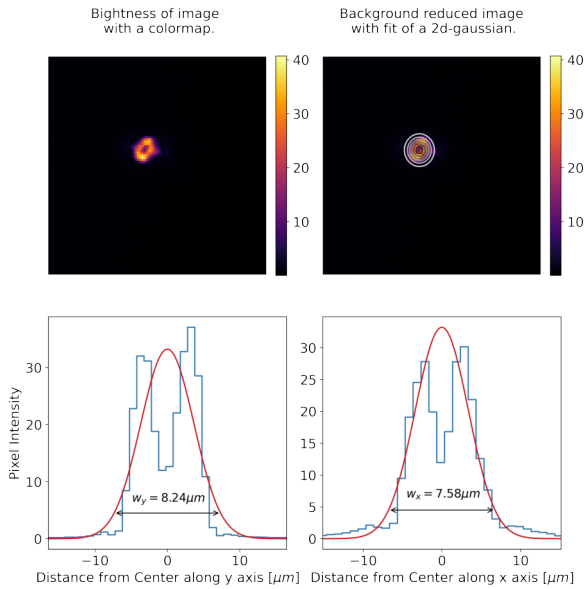

FIGURE 3.13: An example of a Gaussian fit, in the presence of rings.

FIGURE 3.14: Figures 3.12 and 3.13 show the fitting that was done on the images taken. In the top left the brightness of an averaged picture is shown. In the top right, we can see the fitted 2D-Gaussian distribution. The plots in the lower column show a slice along the x and y direction of a 1D-Gaussian distribution.

can be seen, respectively. In general, the fit does not seem perfect. The error bars of the position arise because the stage was labeled only every 10 µm so we assumed an error of ±2.5 µm. The measured beam sizes are

$$w_x = 2.4 \pm 1.7\,\mu\text{m} \tag{3.5}$$

and

$$w_y = 1.7 \pm 0.9\,\mu\text{m} \tag{3.6}$$

As can be seen, the error bars are quite large compared to the spot size. Because the beam shape is not Gaussian, we observe that equation 2.40 is not an exact description of the actual beamwidth and will underestimate the beam width at the focus. The more points larger away from the focus

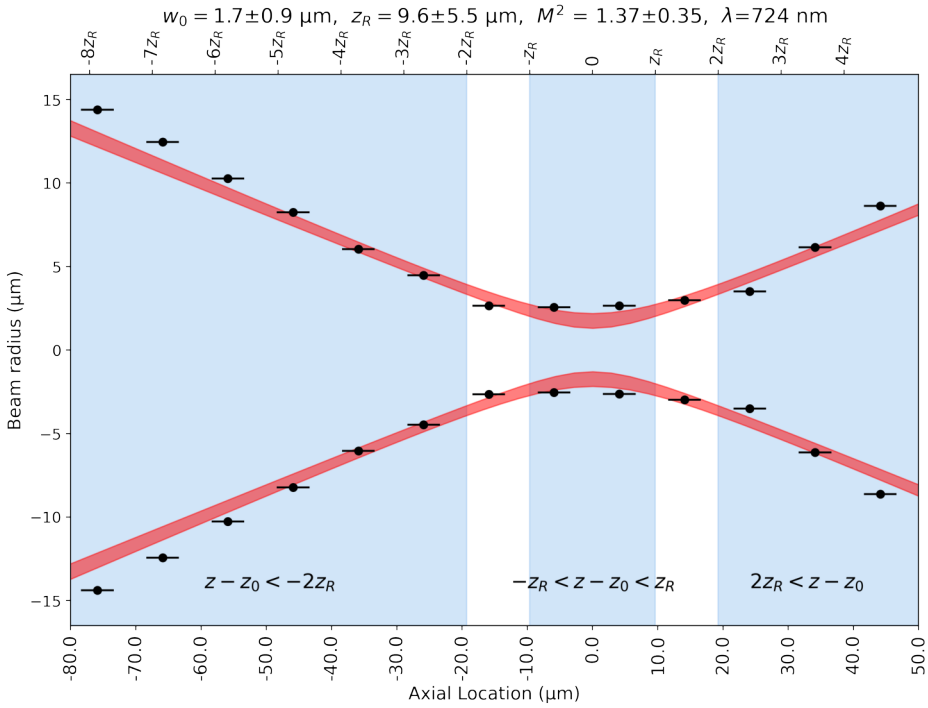

(A) Measuring beam waist along the vertical direction.

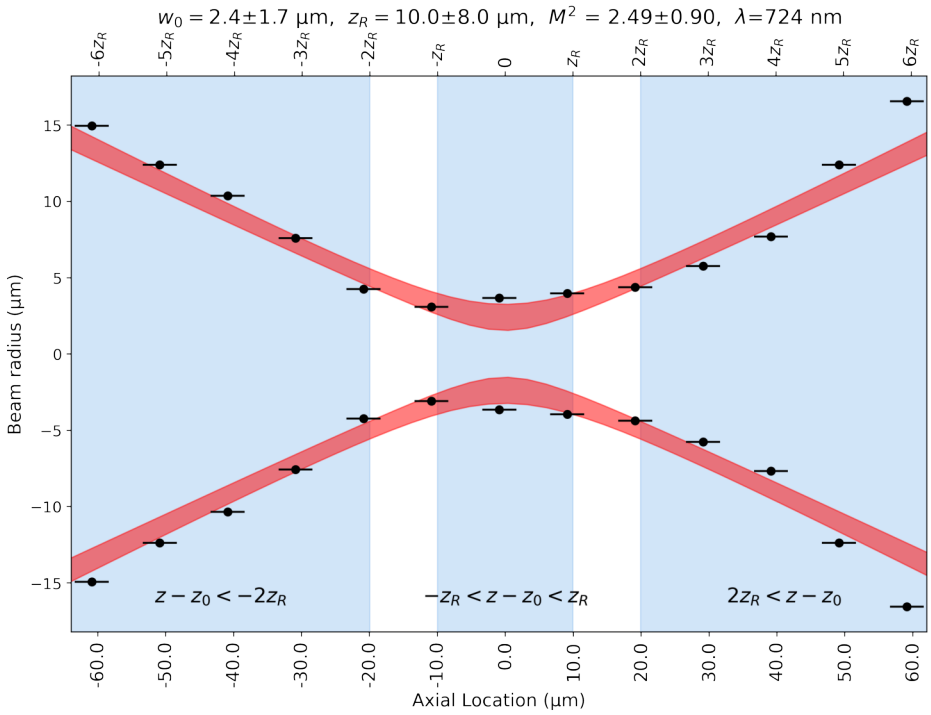

(B) Measuring beam waist along the horizontal direction.

FIGURE 3.15: The points correspond to the fitted waists of the beam. The error bars denote the uncertainty in the distance to the focal plane. The red plot is the fitted beam waist using equation 2.40 with error bars. The background in white is used to show the Rayleigh range of the beam. The title denotes the fitted beam waist w_0, the Rayleigh range z_R, the beam quality factor M^2, and the wavelength λ of the laser beam that we used.

are taken into consideration the more this formula will underestimate the actual spot size. Still, this measurement shows that it should be possible to address a single ion. At this point during my thesis the ion trap was also prepared in the vacuum chamber and we moved the single-ion addressing setup so that we can direct the light into the trap. The following measurements in chapter 4 were made by addressing ions. We reimaged the Gaussian beam using ions, see section 4.3.

4 Single-ion addressing

4.1 The ion trapping setup

This chapter will describe experiments that were performed on the main setup. At the heart of the setup sits the 3d Paul trap. An image of the trap is shown in figure 4.1. Next to the trap is an oven filled with Calcium powder with its opening pointing toward the trap. By applying a voltage to the oven the Calcium heats up and flies into the trap. There we ionize it in a 2−level process, see section 2.1, and trap them in the Paul trap. We apply radio frequency to trap the ions and tune the DC-Voltages so that the ions sit at the minimum of the oscillating electric field generated by the radio frequency, to minimize the micro-motion of the ion. The Paul trap is surrounded by a baked-out vacuum chamber that is continuously being pumped by an ion pump.

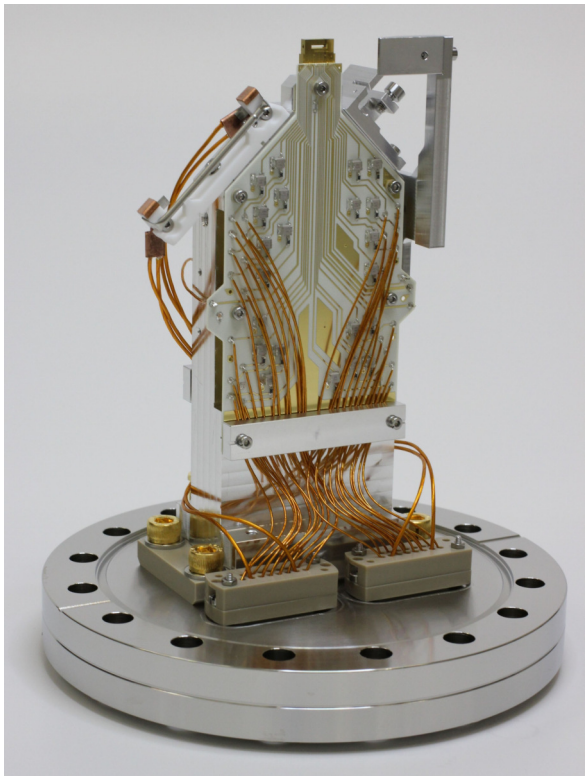

FIGURE 4.1: Picture of the ion trap mounted onto a PCB with DC filter and attached to a CF100 vacuum flange.

Figure 4.2 shows a sketch with the essential components of the experimental setup. Because the light coming from the single-ion addressing setup has a wave vector perpendicular to the trap axis, we also utilize another beam, going horizontally into the trap. This way we can also measure the axial motion of the ions spectroscopically. We also used this beam to observe the first quantum jumps. This way we already calibrated the frequency of the addressing light on one of the qubit transitions before aligning the setup. We then also managed to observe quantum jumps using the light going through the AODs. Initially, the trap was not in the focus plane of the single-ion addressing beam. Because of the small Rayleigh range of the tightly focused spot, the laser beam was quite large compared to its size at the focus and it was not difficult to also see quantum jumps using the single-ion addressing setup. To bring the focus plane of the beam in line with the trap axis we applied a short pulse of light while reading out the ion repeatedly, and aimed to minimize the population p_s by adjusting the distance of the focusing objective to the ion trap. After each adjustment of this distance, we would beam walk using the mirror at the end of the telescope and the dichroic mirror to move the peak of the intensity distribution of the laser beam on the ion and align it centrally through the objective.

Once the focus plane was close to the position of the ion, we also utilized the AODs to continuously scan horizontally or vertically, depending on the direction of the beam walk. This way we would know in which direction to adjust the position of the objective. Switching between adjusting

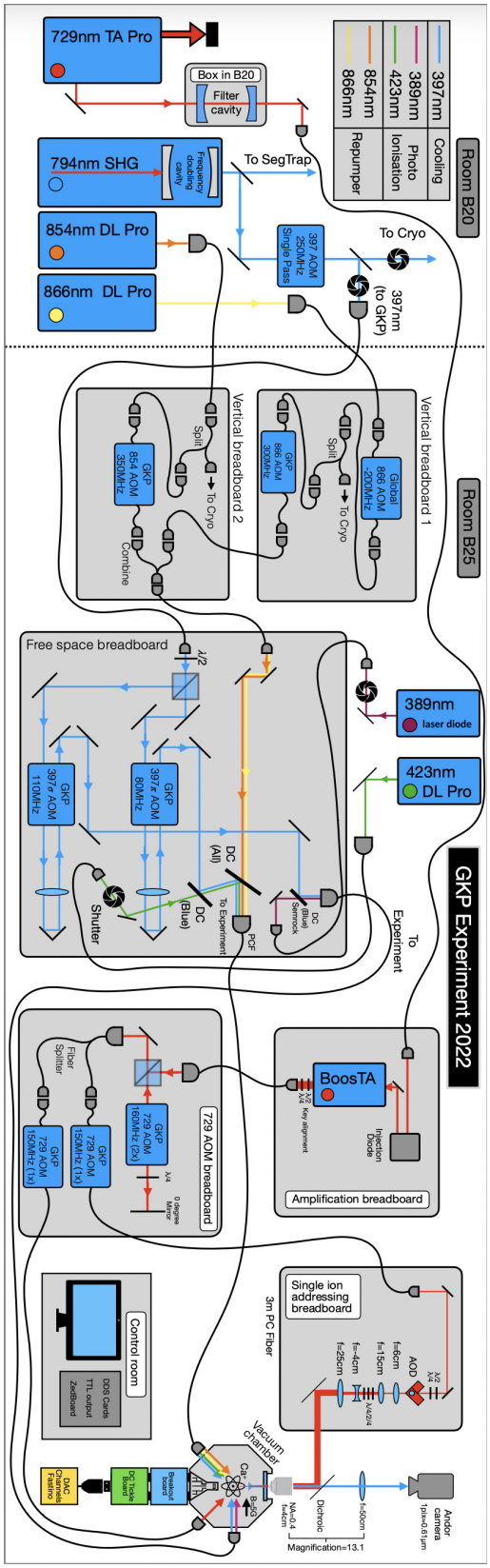

FIGURE 4.2: Schematic drawing of the experimental setup. For a detailed description of the tapered amplifiers setup, see [10]. Created by Stephan Welte.

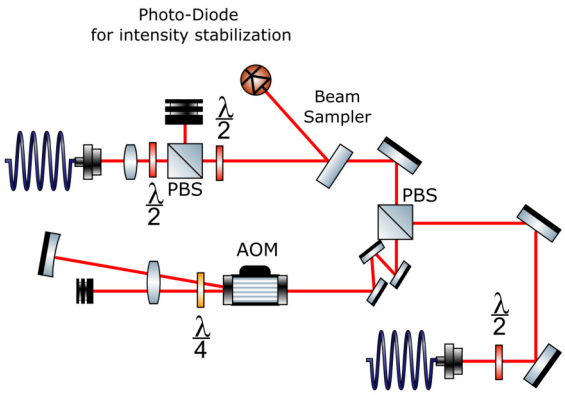

FIGURE 4.3: Scheme of the double pass setup. The light is coming from the boosTA, see figure 4.2 and goes towards a single-pass fiber AOM and then to the single-ion addressing setup.

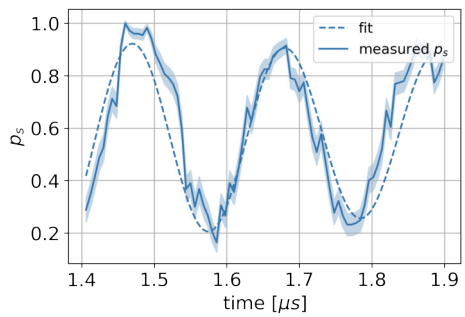

FIGURE 4.4: Rabi oscillations measured with maximal power at the peak of the intensity. The light is not resonant with the Stark-shifted transition. The measurement does not start with pulses shorter than 1.4µs, because this was not implemented in the control system at the time. The shaded area denotes the uncertainty according to equation 2.5.

the position of the objective along the laser beam and beam walking using the mirror we could maximize the Rabi frequency of the qubit transition. The Rabi flops after aligning the single-addressing setup can be seen in figure 4.4. They are recorded before we implemented a full set of calibration measurements. EIT cooling was also not yet implemented. When fitting it with equation 2.29 with an exponential decay modeling the thermal distribution the Rabi frequency we observe is

$$\Omega_0 = 29.9 \pm 0.3\,\text{MHz}. \tag{4.1}$$

We did not repeat measurements of these high Rabi frequencies because we subsequently split the addressing light between the single-addressing setup and an additional diagonal beamline, see figure4.2.

4.2 Individual addressing of ions

In an experiment, we usually perform a series of cooling steps, followed by the specific laser sequence for the experiment, followed by the readout. In this thesis, the main experiments were performed with the generic experimental sequence shown in figure 4.5. Depending on the experiment we might change the frequency of the light or position of the laser beam by changing the frequencies applied to the AODs at different steps. First, we cool the ions using Doppler cooling. Then, we further reduce the temperature of the ion using EIT cooling, see section 2.4. We then initialize the state in the

$S_{\{1/2,1/2\}}$ level by applying σ^+ polarized light. The 854nm beam is turned on during state preparation in case we also sideband cool the ion beforehand. We did not utilize sideband cooling for any measurements presented in this thesis. Afterward, we drive the $S_{\{1/2,1/2\}} \leftrightarrow D_{\{5/2,5/2\}}$ transition and read out the qubit state.

To measure the spectrum seen in 4.6 we changed the polarization of the addressing beam to be

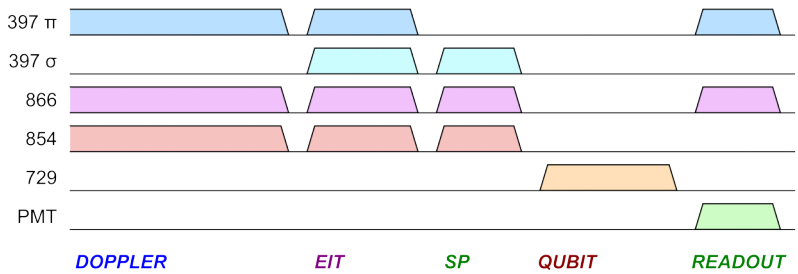

FIGURE 4.5: Scheme of the experimental sequence. We perform Doppler- and EIT cooling followed by state preparation. We then drive the qubit transition and read out the quantum state. Specific detunings and times depend on the specific experiment.

able to drive transition with $\Delta m = \pm 1$ and $\Delta m = \pm 2$. At this point, only Doppler cooling was implemented. We then varied the frequency of the addressing beam and measured the population in the S state p_S. We identified the peaks of the possible transitions between the $S_{1/2} \leftrightarrow D_{5/2}$ manifold. All other peaks are either sidebands or servo bumps.

4.3 Using ions to image the laser beam with high resolution

During calibration of the laser position, we noticed that it might be useful to scan the AODs independently of each other, to move the beam over a 2-dimensional area over the ion. This way we can find the peak intensity of the laser beam. By scanning the beam in 2 dimensions it is also possible to image the intensity distribution.

First, we defined new frequencies that take the input frequencies for the AODs and rotate them by 45°. This way we can steer the laser beam horizontally and vertically over the position of the ion. This way we can the beams horizontally or vertically so that by scanning these variables independently of each other we can point the laser beam over a rectangular area without any distortions. They are

$$f_{\text{hor}} = \frac{f_{\text{aod1}} + f_{\text{aod2}}}{\sqrt{2}} \tag{4.2}$$

$$f_{\text{vert}} = \frac{-f_{\text{aod1}} + f_{\text{aod2}}}{\sqrt{2}}, \tag{4.3}$$

where $f_{\text{aod1,2}}$ are the frequencies applied to the AODs. On any point not on the horizontal axis, frequency shifts by the individual AODs do not cancel each other out, so we used the double pass AOM to compensate for the frequency shift. Then we tune

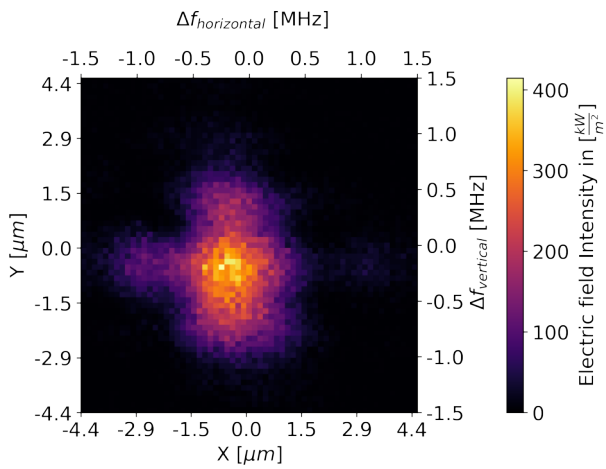

FIGURE 4.7: Using an ion to image a laser beam in high detail. The radio frequencies we scan over are the ones defined in equation 4.2. The electric field intensity has been calculated from the populations using equation 4.4 and 4.5

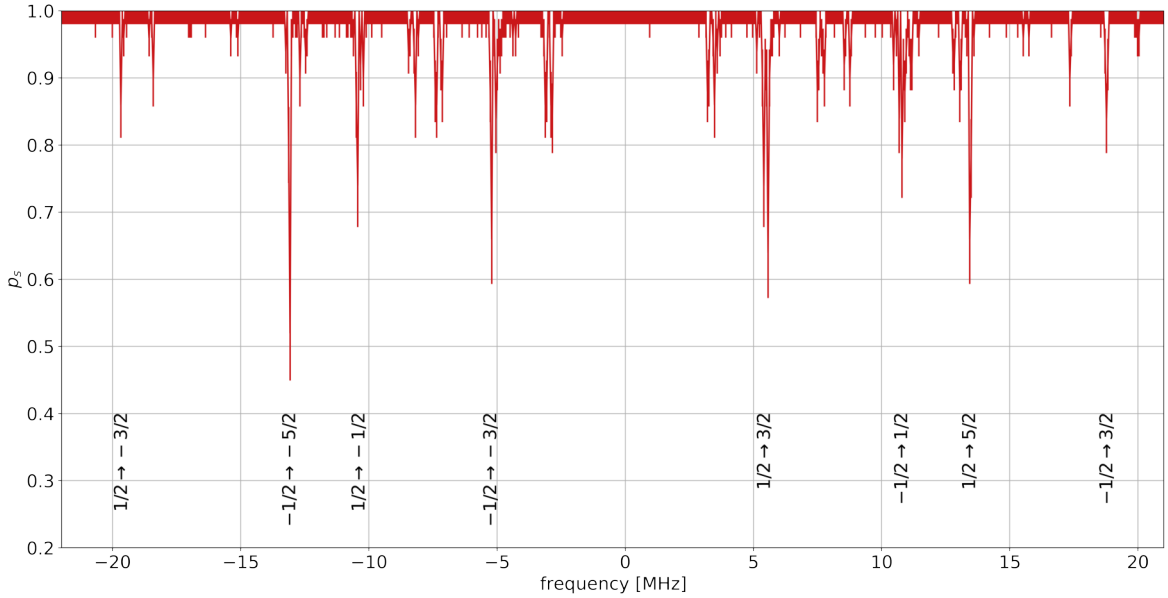

FIGURE 4.6: Spectrum of the $D_{5/2} \leftrightarrow S_{1/2}$ transitions, with the specific transitions between the Zeeman levels identified. The transitions with $\Delta m = 0$ were not addressed, because the laser beam has an angle of 90° to the magnetic field, see equation 2.17. The error bars were calculated using equation 2.5.

the laser frequency to the $S_{\{1/2,1/2\}} \leftrightarrow D_{\{5/2,5/2\}}$ transition. We then scan the newly defined frequency at each point applying the experimental sequence in figure 4.5 50 times. The pulse time for which we drive the qubit transition must not exceed the π-time at the peak of the intensity distribution of the laser beam. This way we get a rectangular map of populations p_S of the ion being in the S-manifold. By calculating the Rabi rate from the population we can thus map the populations to the electric field amplitude. Given that the Rabi oscillations are described by equation 2.30 we can solve for the Rabi frequency

$$\Omega = \arccos\left(-2p_S + 1\right) / t_{pulse}. \tag{4.4}$$

By setting $t_{pulse} < t_\pi$ we measure populations on the slope of the first Rabi flop. This means the p_S that we measure are monotonic. Knowing the transition we address we can also calculate the electric field. In our case this is the $S_{\{1/2,1/2\}} \leftrightarrow D_{\{5/2,5/2\}}$ transition so that the Rabi frequency is given by equation 2.18 with $\Gamma = 1.38 \times 10^{-7}(2\pi \cdot \mathrm{MHz})$, so that

$$E = \frac{\hbar\Omega}{e}\sqrt{\frac{64\pi^3 c\alpha}{5\lambda^3\Gamma}}. \tag{4.5}$$

By squaring the electric field amplitude we find the electric field intensity of the laser beam by driving Rabi oscillations on an ion. We did not take into account the optical Magnus effect, due to which the polarization of the light might change in a tightly focused beam in the flanks of the beam in the focal plane [40], [41]. There have been proposals to use this effect to implement a quantum gate for a beam waist of $w_0 \approx 0.5\,\mu\mathrm{m}$ [42].

One such scan over a rectangular area with populations transformed to electric field intensity can be seen in figure 4.7. To know the scale in meter that we scan over we use the distance between ions as a calibration parameter. We load two ions and use the same technique described above to measure the distance between the two peaks of the intensity distributions which corresponds to the positions of the ions. It would also be possible to scan the beam only horizontally. Using a two-dimensional scan it is possible to additionally measure the angle between the horizontal axis of the AODs and the trap axis and correct for it. As can be seen from figure 4.8 they do not match exactly. We load two ions and measure the distance between them in frequency applied to the AODs. We then calculate the distance of the two ions assuming a harmonic potential. By comparing the distances we get a calibration rate in distance/frequency.

We assume that two ions are trapped in a Paul trap and are confined along the trap axis by a harmonic potential. Here, z goes along the trap axis. Then each ion is at position $\pm\frac{z_0}{2}$, respectively, their distance is z_0. There are two forces acting, the force acted by the harmonic potential $|F_H|$ and the Coulomb force $|F_q|$:

$$|F_H| = kx = \omega_z^2 m \frac{z_0}{2} \tag{4.6}$$

with $\omega_z = \sqrt{\frac{k}{m}}$ and

$$|F_q| = \frac{e^2}{4\pi\epsilon_0 z_0^2}. \tag{4.7}$$

Then in steady state $F_H = F_q$, so

$$z_0^3 = \frac{2e^2}{4\pi\epsilon_0 m w_0^2}. \tag{4.8}$$

The scan we used to calibrate the ration can be seen in figure 4.8. We then use the additional axial beamline to measure the axial sideband. At the time of the measurement it was

$$w_0 = 2\pi \times 766\,\text{kHz} \tag{4.9}$$

Using equation 4.8 we find that the distance between the ions is

$$z_0 = 6.695\,\mu\text{m}. \tag{4.10}$$

Fitting two Gaussian distributions on the data shown in figure 4.8 we find that the distance between the distributions is 2.292MHz in radio frequency applied to the AODs. This means that we find a calibration between the applied radio frequency and distance at the trap

$$\text{cal} = 2.92\,\frac{\mu\text{m}}{\text{MHz}}. \tag{4.11}$$

We also calculate the angle between the horizontal axis of the AODs and the trap axis which is 2° which we correct using the Goniometer We can use the calibration parameter to translate the bandwidth of the AODs, see table 3.1, into an addressing range and find that it is 110 MHz wide. We can now measure the beam waist of the addressing beam using the method as described and compare it with the earlier measurement using the raspberry pi camera. The result can be seen in figure 4.9. The beam waists according to the 2-dimensional Gaussian fit are

$$w_x = 1.96 \pm 0.1\,\mu\text{m} \tag{4.12}$$

and

$$w_y = 2.69 \pm 0.2\,\mu\text{m}. \tag{4.13}$$

Although we did cannot say for certain whether we took this image in the focus plane (the error bar might be up to 5µm either way) the values do agree with the previous measurements. It is interesting to note that the long axis of the ellipse is now in the vertical direction rather than the horizontal one like before. We did not manage to align the setup perfectly by reducing all aberrations. We then decided that it is more useful to have a smaller waist along the horizontal axis than the vertical axis to reduce the crosstalk. Because of the aberrations, the Gaussian fit underestimates the beam waist along the horizontal direction. As we can see from figure 4.7, we can take very detailed images of the beam with higher resolution than any camera could, without using any extra optics to image it. Using this method our idea was to find out more about the beam shape and possibly characterize the aberrations of our system.

4.4 Extended Nieboer Zernike theory

We have seen that we can use the measurement displayed in figure 4.7 to essentially picture the laser beam with a very high resolution. This would not be possible with any camera without using

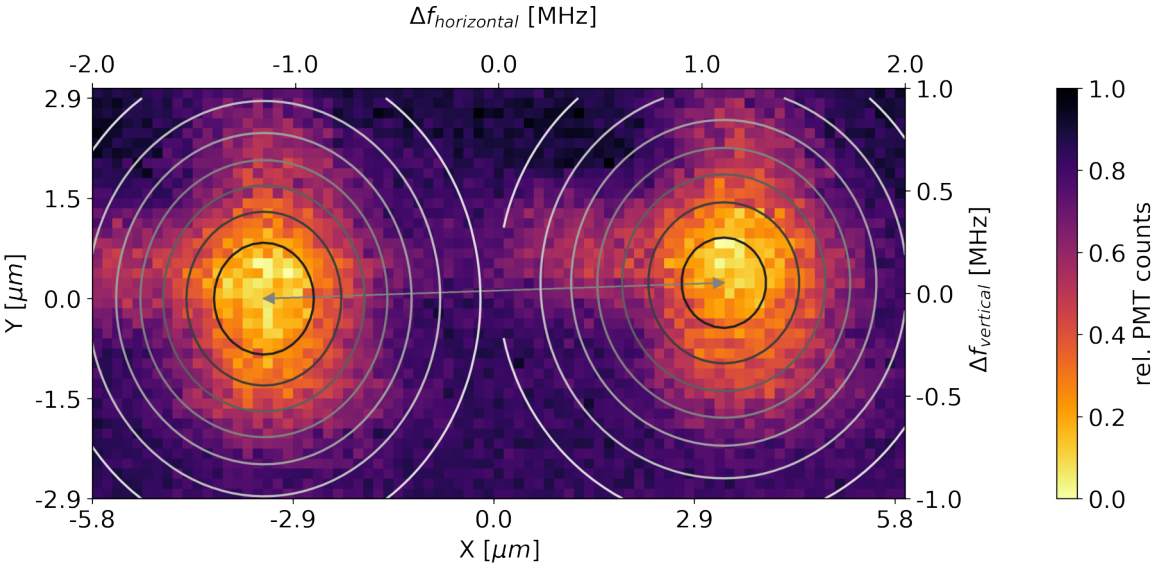

FIGURE 4.8: Measurement to calibrate the ratio between laser spatial displacement and AOD frequency. The radio frequencies we scan over are the ones defined in equation 4.2. We fit the intensity distributions with a 2d-Gaussian and measure the distance between the peaks. The distances in µm are calculated using the calibration parameter 4.11.

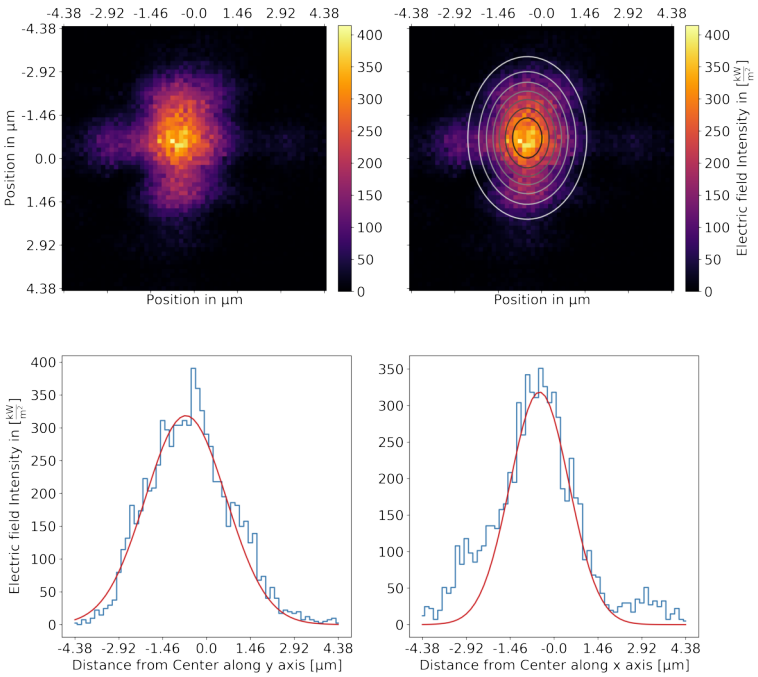

FIGURE 4.9: Measurement of the beam waist using the ion

additional optics to image the laser beam, because the focus is on the order of micrometers. This possibility leads us to the idea to use these high-resolution images to find out more about the setup that we are using and potentially improve both the alignment and overall design. Concretely, we wanted to use the extended Nieboer-Zernike theory to find out the aberrations in our setup using intensity measurements taken around the focal plane. First, we will present the overall theory as developed in [43], [44] and [45]. We will focus on the derivation for a Gaussian beam which was already mentioned in their work.
Recall equation 2.35, the electric field of a Gaussian beam with a k-vector in the x direction is given by:

$$\tilde{E}(r,z) = E_0 \frac{w_0}{w(z)} \exp\left(\frac{-r^2}{w(z)^2}\right) \exp\left(-i\left(kz + k\frac{r^2}{2R(z)} - \psi(z)\right)\right) \tag{4.14}$$

Assuming that the beam is collimated well enough, we assume that the beam waist w_0 is constant and the curvature is negligible. Then we can approximate a Gaussian beam:

$$\tilde{E}(r) = E_0 \exp\left(\frac{-r^2}{w_0^2}\right) \exp\left(-i\left(kz_0 - \psi(z_0)\right)\right). \tag{4.15}$$

It differs from a plane wave only in its intensity distribution and constant phase factor. A general diffraction in the Fresnel approximation for a perfect lens is given by [26]:

$$g(r,\phi) = \frac{i}{\lambda z} \exp(-ikz) \exp\left(-i\pi\frac{r^2}{\lambda f^2}\right) F\left(\frac{r}{\lambda f},\theta\right). \tag{4.16}$$

Here $F(r,\phi)$ is the Fourier transform of the input function $f(\rho,\theta)$, in our case the Gaussian beam. A general Fourier Transformation in polar coordinates is given by:

$$F(r,\phi) = \int_0^{\infty}\int_{-\pi}^{+\pi} f(\rho,\theta) \exp\left(-ir\rho(\cos(\theta-\phi)\right) d\theta d\rho \tag{4.17}$$

To investigate the aberrations we assume that the lens is not perfect and describe the imperfections by a pupil function $P(r,\theta)$, that will describe the aberrations. The most general pupil function is given by:

$$P(\rho,\theta) = A(\rho,\theta) \exp i\Phi(\rho,\theta) \tag{4.18}$$

We now assume that the transmission function A is 0 outside of the lens and that we can describe general aberrations with real Φ. This will make the retrieval algorithm mathematically simpler and allows us to find a simple algorithm for the aberration retrieval by solving a linear system of equations. Now we want to normalize the expression, by setting the coordinates in the image plane to $\tilde{r} = r\frac{NA}{\lambda}$ and by normalizing the coordinates in the plane of the lens so that the radius of the lens is 1. By normalizing the whole expression we find the starting expression in [46]:

$$E(r,\phi) = \frac{1}{\pi}\int_0^1\int_0^{2\pi} \rho \exp\left(i\rho^2 f\right) P(\rho,\theta+\phi) \exp\left(2\pi i\rho r\cos\theta\right) d\theta d\rho$$

with a defocus parameter that is $f = -2\pi z$ for plane waves but is

$$f = -2\pi\frac{1-\sqrt{(1-NA^2)}z}{2\lambda} + i\frac{R^2}{w^2} \tag{4.19}$$

for a Gaussian beam in our approximation with R being the radius of the lens so that the beam waist at the lens is normalized. Now we can expand the phase aberrations. For the general case

$$P(\rho,\theta) = \sum_{n,m} \beta_n^m Z_n^m(\rho,\theta) \tag{4.20}$$

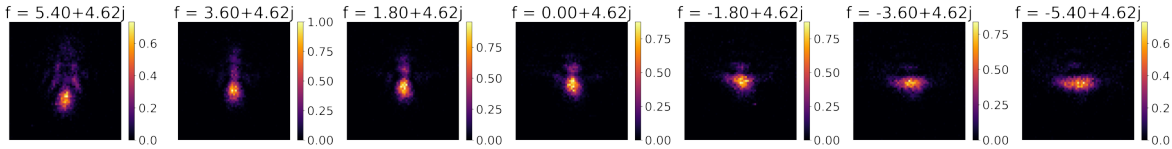

(A) Measured Rabi oscillations converted to intensities, the title denotes the defocus parameter according to equation 4.19.

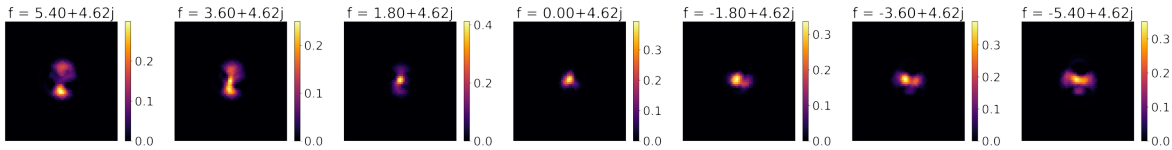

(B) Simulated intensities calculated from retrieved phase aberrations.

FIGURE 4.10: Comparison of measured intensities (A) versus simulated intensities using retrieved aberration coefficients (B).

where β is a complex number and $Z_n^m = R_n^m(\rho)\cos(m\theta)$. In the simpler case we only assume phase aberrations and can expand the exponent Φ in real coefficients:

$$\Phi(\rho,\theta) = \sum_{n,m} \alpha_n^m Z_n^m(\rho,\theta) \tag{4.21}$$

Then we proceed by expanding Eq. 4.19 in orders of Φ and evaluating the integral over θ:

$$\begin{aligned}\int_0^{2\pi} \quad & \Phi(\rho,\theta+\phi)\exp\left(2\pi i\rho r\left(\cos(\theta)\right)\right)d\theta \\ &= \sum_{n,m}\alpha_n^m R_n^m(\rho)\int_0^{2\pi}\cos(m(\theta+\phi))\exp\left(2\pi i\rho r\left(\cos(\theta)\right)\right)d\theta \\ &= 2\pi\sum_{n,m}\alpha_n^m i^m R_n^m(\rho)J_m(2\pi\rho r)\cos(m\phi)\end{aligned} \tag{4.22}$$

The following has been taken from [44] and can be seen in full detail there. Then we can find an expression for the electric field:

$$E(r,\varphi;f) \approx 2V_0^0(r,f) + 2\mathrm{i}\sum_{n,m}\mathrm{i}^m\alpha_n^m V_n^m(r,f)\cos m\varphi \tag{4.23}$$

where

$$V_n^m(r,f) = \int_0^1 \rho\exp\left(\mathrm{i}f\rho^2\right)R_n^m(\rho)J_m(2\pi r\rho)\mathrm{d}\rho \tag{4.24}$$

$$= \exp(\mathrm{i}f)\sum_{l=0}^{\infty}\left(\frac{-\mathrm{i}f}{\pi r}\right)^l\sum_{j=0}^{p}u_{lj}\frac{J_{m+l+2j+1}(2\pi r)}{2\pi r} \tag{4.25}$$

with coefficients

$$u_{lj} = (-1)^p\frac{m+l+2j+1}{q+l+j+1}\binom{m+j+l}{l}\binom{j+l}{l}\binom{l}{p-j}\Big/\binom{q+l+j}{l}, \tag{4.26}$$

The full derivation can be found in [45] and linked references therein. That means the electric field intensity is given by

$$I \approx 4\left|V_{00}\right|^2 + 8\sum_{nm}\alpha_{nm}\,\mathrm{Re}\left\{i^{m+1}V_{00}^*V_{nm}\right\}\cos m\phi \tag{4.27}$$

We want to find the aberration coefficients α_{nm} given that we can measure the intensity for different values of f, that means at different distances to the focus. Our goal is to find an algorithm that extracts these αs. In the first step, we can do a harmonic analysis for the even part of the angular dependence.

In the same way, we can find the uneven contributions by using a sine wave in the harmonic analysis.

$$\Psi^m(r,f) = \frac{1}{2\pi}\int_0^{2\pi} I(r,\phi,f)\cos m\phi d\phi. \tag{4.28}$$

We then define an inner product:

$$(\Psi,\chi) = \int_0^R \int_{-F}^F r\cdot\Psi(r,f)\cdot\chi(r,f)^*\,\mathrm{d}r\,\mathrm{d}f. \tag{4.29}$$

with

$$\Psi_n^m(r,f) = \gamma_m \operatorname{Re}\left\{i^{m+1}V_{00}^* V_{nm}\right\}, \tag{4.30}$$

where $\gamma_m = 4, m = 1,2,\cdots,\gamma_0 = 8$. Then by multiplying equation 4.27 by $\cos m\phi$ and integrating over ϕ, we can express the m'th harmonic term of the observed intensity in the form of a sum over $\Psi_n^m(r,f)$'s with coefficients α_{nm}:

$$\sum_n \alpha_{nm}\Psi_n^m(r,f) \approx \Psi^m(r,f) \tag{4.31}$$

This way we can approximate measured Ψ^m's on the right by functions involving the Zernike coefficients on the left. We can solve these linear systems of equations

$$\sum_n \alpha_{nm}\left(\Psi_n^m,\Psi_{n'}^m\right) = \left(\Psi^m,\Psi_{n'}^m\right) \tag{4.32}$$

We then choose the number of n' parameters to be M. We can then solve this $M\times M$ linear system. The solution is the best linear combination that one can obtain from the experimentally observed intensity profile using M terms.

In Appendix B we show that the algorithm works while including he modified defocus parameter f to incorporate the Gaussian beam shape into the model, see equation 4.19. We can retrieve small aberrations with high precision. Applying the same method to actual data, as seen in subfigure 4.10(A) extracts aberrations on the order of 10 which does not agree with the model's capabilities. It is meant to retrieve aberrations that are $\ll$ so that the expansion in Φ works. Although they can qualitatively capture the beam shape it was not possible to use this method that relies on small phase aberrations to retrieve aberrations of our setup. It might be possible to use an extended method mentioned in [44] to account for not only phase aberrations but also modulations of the amplitude. The full implementation of other methods was outside the scope of this work.

4.5 Beam-pointing error

To individually address single ions, we designed a tightly focused beam, such that the spot size is small compared to the ion-ion distance. This also means that any movement of the beam might affect the beam position compared to the ion. The ion will see different electric field amplitudes which will lead to different Rabi frequencies. Because the electric field magnitude is approximately Gaussian in space this will lead to larger fluctuations at the flank of the beam where we would sample over a larger range of the electric field magnitude, because of a larger slope of the electric field amplitude. For every experimental data point, we have to do statistics over several experimental shots to get information about the quantum state. If the beam moves we sample over different Rabi frequencies at the ion. This will lead to a decaying amplitude of the Rabi oscillations.

To quantify the beam pointing error we will assume a noise model, then calculate a model for the decay of the Rabi oscillations and compare it to the experiment. We derived the following model after talking to Alfredo Ricci and taking his work towards [47] into account.

We assume that the beam will fluctuate around a point x_0, where the Rabi frequency is Ω_0. We can model the fluctuations by a probability distribution from which we sample. For different shots of the experiment, the Rabi frequency will be sampled around Ω_0. We will assume that the probability for each Rabi frequency will follow a normal distribution with mean Ω_0 and standard deviation

σ. We will assume that the Rabi rate will stay constant during one shot. Then, the Rabi frequency of each shot (n) will be

$$\Omega_n = \Omega_0 + \Omega_i \tag{4.33}$$

Here $\Omega_n \propto N(\Omega_0, \sigma^2)$ so that $\Omega_i \sim N(0, \sigma^2)$, denoting a normal distribution with mean 0 and standard deviation σ.

The probability for each Ω_i is $p_i = \frac{1}{\sqrt{2\pi\sigma^2}} e^{-\Omega_i^2/2\sigma^2}$. The probability c_0 of detecting state $|0\rangle$ state will therefore be

$$c_0 = \int_{\Omega_i} p_n \cos^2(\Omega_n t/2) d\Omega_i \tag{4.34}$$

$$= \frac{1}{2} + \frac{1}{2} \int_{\Omega_i} p_n \cos(\Omega_n t) d\Omega_i \tag{4.35}$$

$$= \frac{1}{2} + \frac{1}{2} \int_{\Omega_i} p_n \cos(\Omega_o t + \Omega_i t) d\Omega_i \tag{4.36}$$

Using the trigonometric identity

$$\cos(A + B) = \cos(A)\cos(B) - \sin(A)\sin(B) \tag{4.37}$$

and identifying that the second integral is an uneven function (because p_n is even) we bring the integral into a form that we can solve:

$$c_0 = \frac{1}{2} + \frac{1}{2} \int_{\Omega_i} p_n \cos(\Omega_o t)\cos(\Omega_i t) d\Omega_i - \frac{1}{2} \int_{\Omega_i} p_n \sin(\Omega_o t)\sin(\Omega_i t) d\Omega_i \tag{4.38}$$

$$= \frac{1}{2} + \frac{1}{2}\cos(\Omega_o t) \int_{\Omega_i} p_n \cos(\Omega_i) d\Omega_i - \frac{1}{2}\sin(\Omega_o t) \int_{\Omega_i} p_n \sin(\Omega_i) d\Omega_i \tag{4.39}$$

$$= \frac{1}{2} + \frac{1}{2}\cos(\Omega_o t) \int_{\Omega_i} p_n \cos(\Omega_i) d\Omega_i \tag{4.40}$$

Inserting p_n we calculate the integral:

$$c_0 = \frac{1}{2} + \frac{1}{2}\cos(\Omega_o t) \int_{\Omega_i} \frac{1}{\sqrt{2\pi\sigma^2}} e^{-{\Omega_i}^2/2\sigma^2} \cos(\Omega_i t) d\Omega_i \tag{4.41}$$

$$= \frac{1}{2} + \frac{1}{2} e^{-\frac{1}{2}\sigma^2 t^2} \cos(\Omega_o t). \tag{4.42}$$

In our case the Rabi frequency is dependent on the position, we can then expand it around x_0

$$\Omega_n(x_n) = \Omega(x_0) + \left.\frac{\partial \Omega}{\partial x}\right|_{x_0} x_i = \Omega_0 + \Omega' x_i \tag{4.43}$$

where Ω' is the gradient of the Rabi frequency with respect to position, evaluated at x_0. Comparing with eq. 4.33 we find that $\Omega_i = \Omega' x_i$. Accordingly the standard deviation of x_i is σ_x, such that $\sigma = \Omega' \sigma_x$. We can thus express the standard deviation of the assumed normal distribution in the position domain.

$$c_0 = \frac{1}{2} + \frac{1}{2} e^{-\Omega'^2 t^2 \sigma_x^2/2} \cos(\Omega_o t) \tag{4.44}$$

Which can be re-written as

$$c_0 = \frac{1}{2} + \frac{1}{2} e^{-\delta^2 t^2/2} \cos(\Omega_o t), \tag{4.45}$$

where

$$\delta = \Omega' \sigma_x \tag{4.46}$$

is the fitted parameter for each Rabi oscillation. Then by calculating Ω' for each x, and comparing δ vs x one can fit the σ_x parameter. In the experiment, we point the beam along the trap axis. Each

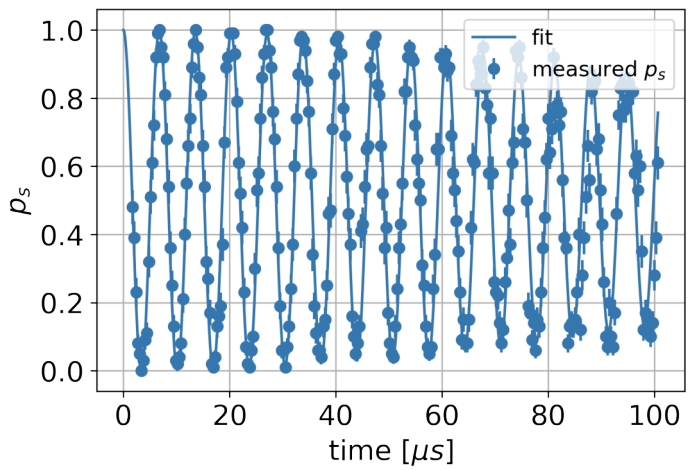

FIGURE 4.11: Fitting the decay along the Rabi oscillations at the center of the beam. The error bars are calculated using the quantum projection noise, see equation 2.5

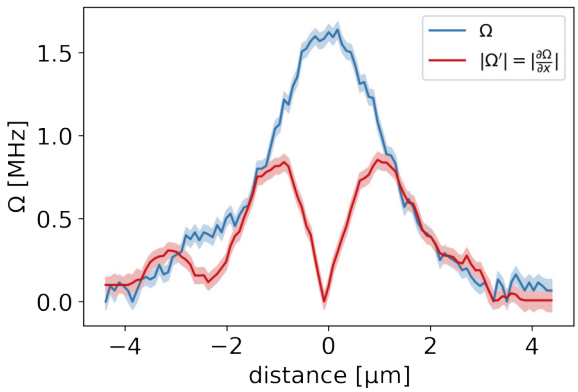

FIGURE 4.12: Characterizing the beam pointing error. The Rabi oscillations have been measured, as described in section 4.3. The derivative has been numerically calculated. The shaded areas indicate the measurement error.

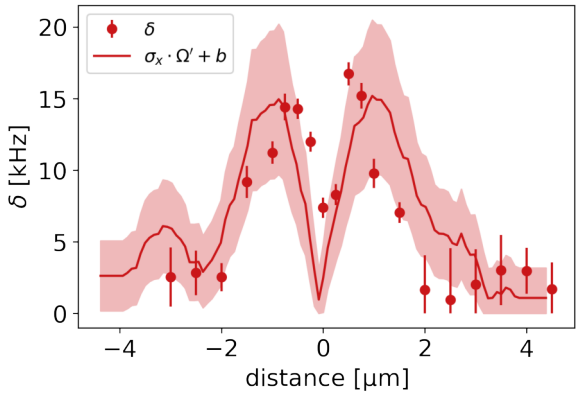

FIGURE 4.13: On the x-axis the distance between the focus of the addressing beam and the ion is plotted. For each point, we fit the decay as in figure 4.11. Then we fit equation 4.46 with an extra offset, the shaded areas indicate the standard deviation of the fit.

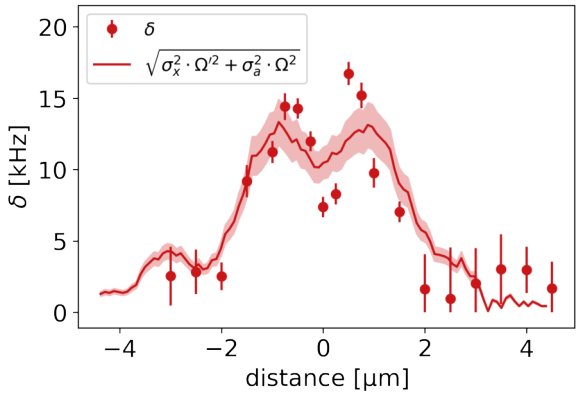

FIGURE 4.14: On the x-axis the distance between the focus of the addressing beam and the ion is plotted. For each point, we fit the decay as in figure 4.11. Then we fit equation 4.51 with an extra offset, the shaded areas indicate the standard deviation of the fit.

decay corresponds to a distance between the ion and the focus of the beam. At different distances to the ion, we cool the ion using both Doppler and EIT cooling and drive Rabi oscillations for a time of 100 µs. Every shot is repeated 100 times. We then fit the decay using equation 4.45. One example at the peak of the intensity distribution can be seen in figure 4.11.

In figure 4.13 we can see the results of the measurement. We then plot the extracted decay parameter δ over the position in µm. Assuming that other sources are leading to decay, like intensity fluctuations of the laser or thermal excitation of the ion, we assume an offset to the decay b and fit the derivative of the Rabi frequency with respect to the position, which we derived numerically, with a scaling factor σ_x. The fitted values are

$$\sigma_x = 16.6 \pm 3.8\,\text{nm} \tag{4.47}$$
$$b = 0.9 \pm 2.1\,\text{kHz} \tag{4.48}$$

We can see that there does seem to be a correlation between the derivation of the Rabi frequency and the decay of the Rabi oscillations, but there also seem to be other contributions to the decay that are dependent on the Rabi frequency.

This leads us to develop a different model, where we assume that we also have fluctuations in the Rabi frequency. Thus our model for Ω is

$$\Omega_n = \tilde{\Omega} + \Omega_i \tag{4.49}$$

with $\tilde{\Omega}$ also being normally distributed with $\tilde{\Omega} \propto N(\Omega_0, \sigma_a^2)$. We then follow the same derivation as above but find that

$$\sigma = \Omega' \sigma_x + \Omega \sigma_a. \tag{4.50}$$

That means that the decay parameter δ in 4.45 is equal to:

$$\delta = \sqrt{\Omega'^2 \sigma_x^2 + \Omega^2 \sigma_a^2} \tag{4.51}$$

The result of the fit can be seen in figure 4.14. The fitted parameters are

$$\sigma_x = 12.8 \pm 1.6\,\text{nm} \tag{4.52}$$
$$\sigma_a = 6.4 \pm 0.7 \times 10^{-3} \tag{4.53}$$

This approach produces a better model for the decay at the focus of the beam but seems to underestimate the decay at the flank of the beam.

Even though both models do not seem to model the decay completely, we can still see the effect of the beam position relative to the ion. Pointing the laser beam 0.25 µm shifted with respect to the peak increases the decay up to 50%. This gives us some insight into how well to align the setup in the lab.

4.6 Characterization of the crosstalk

One of the most important characteristics of a single-ion addressing setup is the magnitude of the crosstalk. It is a measure of how well we can address ions individually. The system is designed to address one ion at a time. Still, the other ion will also interact with an electric field because it sits on the tail of the electric field intensity distribution. It is possible to define the crosstalk in several ways:

One way is to measure the intensity distribution of the electric field of the laser beam and compare intensities at different possible positions of the ion. The authors in [48] define this as the intensity crosstalk .

Another way to define crosstalk is by the fidelity of a π-pulse. Assuming we are applying one π-pulse, we will rotate a qubit in ion one from state $|0\rangle$ to state $|1\rangle$ and vice-versa. While the laser is turned on, this will also lead to a rotation on the qubit in the second ion, with the Rabi frequency proportional to the electric field amplitude at the location of the second ion. By measuring the second qubit in the computational basis we can find the probability of the qubit also changing its state. This probability is another way to quantify the crosstalk. In other words, it is the fidelity of the identity operation on qubit 2 dependent on doing a single π-pulse on qubit one. We call this the operational crosstalk.

We can compute both definitions of the crosstalk from one set of measurements: At the moment of the thesis we do not have a system to individually detect ions in place. It is possible to detect the state of more than one ion by use of just a photomultiplier tube, see section 2.2. To measure the crosstalk it is also possible to only have one ion trapped. This ion will take the place of the second ion, while the position of the laser beam is pointed at different possible positions of the first ion. The distance between the ion and the focus of the laser beam denotes the distance two trapped ions would have. We can then measure the crosstalk as a function of the distance between the laser beam and the ion. This way we can reduce the errors of readout.

For every distance we take the following measurement: We tune the addressing light to be on resonance with the $D_{5/2}$-$S_{1/2}$ transition to account for different stark shifts. We thus measure the population transfer for the second ion if we would drive it resonantly. This way we can read out the Rabi frequency Ω_0 as a function of the distance between the laser beam and the ion. This differs from the case for two ions in which the second ion is non-resonantly driven due to a different Stark shift. Due to a strong Stark shift, we observed very low population transfer at distances larger than 5 µm from which we cannot infer the Rabi frequency.

We then cool the ion using Doppler- and EIT-cooling and apply light for our qubit transition $D_{5/2}$-$S_{1/2}$ of increasing length to drive Rabi oscillations. see scheme in figure 4.5. From there we can fit equation 2.29 and extract the Rabi frequency and the detuning. This is done in case the addressing frequency is still slightly detuned. From there we can infer the electric field intensity which scales as $\Omega \propto I^2$ to calculate the crosstalk of the intensity. We can also insert the π-time τ_π at the peak of the distribution into the fitted Rabi oscillations to give us the population transfer that would happen on a second ion. This gives us the population of the second ion being in the $|1\rangle$ state:

$$p_D(x) = \cos^2\left(\frac{\Omega_0(x)}{2}\tau_\pi\right) \tag{4.54}$$

with Ω_0 and Δ fitted and Δ accounted for.

In figures 4.15 and 4.16 the results of the crosstalk measurements can be seen. The calculated prob-

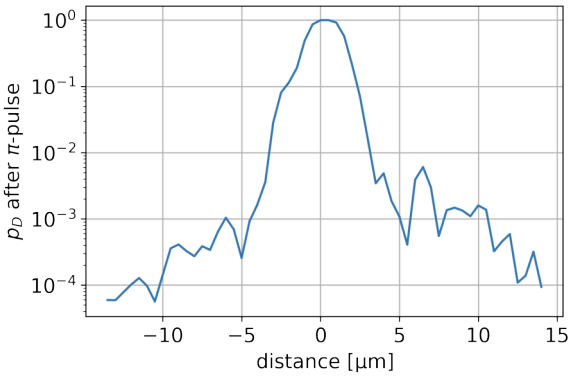

FIGURE 4.15: On the x-axis the distance between the focus of the addressing beam and the ion is plotted, on the y-axis the probability of finding the ion in state $|1\rangle$ after time τ_π see equation 4.54.

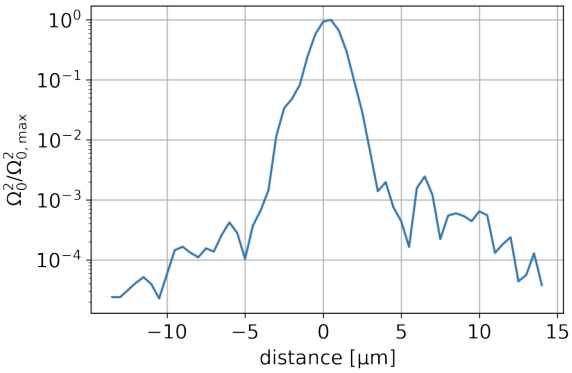

FIGURE 4.16: On the x-axis the distance between the focus of the addressing beam and the ion is plotted, on the y-axis Ω^2 normalized by the Rabi frequency at the focus.

ability of the qubit changing its state is logarithmically plotted over the position of the laser beam. The error bars are of the order of 1% compared to the crosstalk and can thus not be seen.

5 Conclusion and outlook

In this thesis, we progressed from aligning the telescope setup to measuring the crosstalk on ions. We started the thesis by aligning the telescope. We found that the polarization of the light is dependent on the applied radio frequency. We quantified this dependence and calculated that its effect on the Rabi frequency is less than 0.01% over the length of 24 µm along the trap axis.

We set up a raspberry picamera v2 to image the beam with a pixel size of 1.12 µm. We found an intensity pattern around the focus that we would also expect from being diffraction limited. Next, we used the mounted camera as a beam profiler. After setting up an optical system to tune the intensity we were able to measure the intensity along the beam propagation around the focal plane of the beam. The results showed that individual addressing ions should be possible and we moved the addressing board to further characterize it on actual ions.

We aligned the setup and went from observing quantum jumps to observing Rabi frequencies of $\Omega = 29.9 \pm 0.3\,\text{MHz}$, see figure 4.4. We also repeated the measurement of the beam waist by converting measured populations to electric field intensity. We find a beam waist of

$$w_x = 1.96 \pm 0.1\,\mu\text{m} \tag{5.1}$$

and

$$w_y = 2.69 \pm 0.2\,\mu\text{m} \tag{5.2}$$

along the horizontal x- and vertical y- direction, respectively, although a Gaussian fit seems to underestimate the actual beam width. Other single addressing setups have achieved a similar beam size [49], [50], [51], [52].

We did not manage to fully characterize the aberrations in our system by adapting an existing algorithm to account for a Gaussian beam shape. In our case, we do not expect the aberrations to hinder the performance of the addressing setup significantly. If this would be the case, building a setup that includes a spatial light modulator might be advantageous, although this comes at the cost of lower addressing intensity.

We also measured the beam pointing error by comparing the decay of Rabi oscillations depending on the position of the beam relative to the ion. By assuming that we sample from a normal distribution we showed this distribution in position space has a standard variation of

$$\sigma_x = 12.8 \pm 1.6\,\text{nm}. \tag{5.3}$$

Taking into account that the fit seems to underestimate the decay at the flank of the beam we can give an upper estimate of 21 nm by using the fit derived from assuming a constant offset, see equation 4.47.

We finally characterized the crosstalk. Defining the crosstalk as the population transfer of the second qubit while doing a π-pulse on the first qubit we show that it is less than 10^{-3} for ions that are 5 µm apart. This means it is feasible to individually address ions.

The intensity crosstalk has been recently measured for a different single-ion addressing setup [48]. They show intensity crosstalk of 10^{-4} at 4 µm away from the peak compared to $6 \cdot 10^{-4}$ in our setup. They measured the crosstalk using a raspberry picamera v2 while we measured it using Rabi oscillations of the addressed ion.

In the future, we plan to use this setup to prepare GKP states in the motion of two trapped ions. To perform logical gates between GKP states encoded in two modes of motion of the two-ion crystal, individual control of each ion is necessary. This work has brought the capability to address individual ions to the GKP setup which will be a crucial tool in performing a two-qubit GKP gate.

Bibliography

[1] Richard P. Feynman. Simulating physics with computers. *International Journal of Theoretical Physics*, 21(6):467–488, June 1982. doi:10.1007/BF02650179.

[2] Yuri Manin. *Vychislimoe i nevychislimoe.* Sovetskoe radio, Moskva, 1980. Open Library ID: OL14696646M.

[3] P.W. Shor. Algorithms for quantum computation: discrete logarithms and factoring. In *Proceedings 35th Annual Symposium on Foundations of Computer Science*, pages 124–134, November 1994. doi:10.1109/SFCS.1994.365700.

[4] Lov K. Grover. A fast quantum mechanical algorithm for database search. In *Proceedings of the twenty-eighth annual ACM symposium on Theory of Computing*, STOC '96, pages 212–219, New York, NY, USA, July 1996. Association for Computing Machinery. URL: https://dl.acm.org/doi/10.1145/237814.237866, doi:10.1145/237814.237866.

[5] W. K. Wootters and W. H. Zurek. A single quantum cannot be cloned. *Nature*, 299(5886):802–803, October 1982. Number: 5886 Publisher: Nature Publishing Group. URL: https://www.nature.com/articles/299802a0, doi:10.1038/299802a0.

[6] Peter W. Shor. Scheme for reducing decoherence in quantum computer memory. *Physical Review A*, 52(4):R2493–R2496, October 1995. Publisher: American Physical Society. URL: https://link.aps.org/doi/10.1103/PhysRevA.52.R2493, doi:10.1103/PhysRevA.52.R2493.

[7] Daniel Gottesman, Alexei Kitaev, and John Preskill. Encoding a qubit in an oscillator. *Physical Review A*, 64(1):012310, June 2001. Publisher: American Physical Society. URL: https://link.aps.org/doi/10.1103/PhysRevA.64.012310, doi:10.1103/PhysRevA.64.012310.

[8] Christa Flühmann. *Encoding a qubit in the motion of a trapped ion using superpositions of displaced squeezed states*. PhD thesis, ETH Zurich, 2019.

[9] Brennan de Neeve, Thanh-Long Nguyen, Tanja Behrle, and Jonathan P. Home. Error correction of a logical grid state qubit by dissipative pumping. *Nature Physics*, 18(3):296–300, March 2022. Number: 3 Publisher: Nature Publishing Group. URL: https://www.nature.com/articles/s41567-021-01487-7, doi:10.1038/s41567-021-01487-7.

[10] Fontboté Schmidt, Moritz. Towards Improved Control of Grid States in Motional States of Trapped Ions. Master's thesis, ETH Zurich, May 2022.

[11] Ralf Alexander Berner. GKP-Setup Imaging System and Single Ion Adressing with an AOD. Technical report, TIQI, ETHZ, July 2022.

[12] Florian Leupold. *Bang-bang Control of a Trapped-Ion Oscillator*. PhD thesis, ETH Zurich, 2015.

[13] Peter Staanum, Inger S. Jensen, Randi G. Martinussen, Dirk Voigt, and Michael Drewsen. Lifetime measurement of the metastable $3d^{2}D_{5-2}$ state in the $^{40}Ca^{+}$ ion using the shelving technique on a few-ion string. *Physical Review A*, 69(3):032503, March 2004. Publisher: American Physical Society. URL: https://link.aps.org/doi/10.1103/PhysRevA.69.032503, doi:10.1103/PhysRevA.69.032503.

[14] Maciej Malinowski. *Unitary and Dissipative Trapped-Ion Entanglement Using Integrated Optics*. PhD thesis, ETH Zurich, 2021.

[15] A. Burrell. *High fidelity readout of trapped ion qubits*. http://purl.org/dc/dcmitype/Text, Oxford University, UK, 2010. URL: https://ora.ox.ac.uk/objects/uuid:ff74c170-518a-40a5-be85-191ec5bb32d7.

[16] W. M. Itano, J. C. Bergquist, J. J. Bollinger, J. M. Gilligan, D. J. Heinzen, F. L. Moore, M. G. Raizen, and D. J. Wineland. Quantum projection noise: Population fluctuations in two-level systems. *Physical Review A*, 47(5):3554–3570, May 1993. URL: https://link.aps.org/doi/10.1103/PhysRevA.47.3554, doi:10.1103/PhysRevA.47.3554.

[17] Cornelius Hempel. *Digital quantum simulation, Schrödinger cat state spectroscopy and setting up a linear ion trap*. PhD thesis, Leopold-Franzens University of Innsbruck, August 2014.

[18] Manoj Joshi. *Coherent dynamics of trapped ions within and outside the Lamb-Dicke regime*. PhD thesis, Imperial College London, April 2018.

[19] Stephan Timo Gulde. *Experimental Realization of Quantum Gates and the Deutsch-Josza Algorithm with Trapped $^{40}Ca^{+}$ Ions*. PhD thesis, Leopold-Franzens-Universität Innsbruck, March 2003. URL: https://www.quantumoptics.at/images/publications/dissertation/gulde_diss.pdf.

[20] S. H. Autler and C. H. Townes. Stark Effect in Rapidly Varying Fields. *Physical Review*, 100(2):703–722, October 1955. Publisher: American Physical Society. URL: https://link.aps.org/doi/10.1103/PhysRev.100.703, doi:10.1103/PhysRev.100.703.

[21] D. J. Wineland, R. E. Drullinger, and F. L. Walls. Radiation-Pressure Cooling of Bound Resonant Absorbers. *Physical Review Letters*, 40(25):1639–1642, June 1978. Publisher: American Physical Society. URL: https://link.aps.org/doi/10.1103/PhysRevLett.40.1639, doi:10.1103/PhysRevLett.40.1639.

[22] Giovanna Morigi, Jürgen Eschner, and Christoph H. Keitel. Ground State Laser Cooling Using Electromagnetically Induced Transparency. *Physical Review Letters*, 85(21):4458–4461, November 2000. Publisher: American Physical Society. URL: https://link.aps.org/doi/10.1103/PhysRevLett.85.4458, doi:10.1103/PhysRevLett.85.4458.

[23] Regina Lechner, Christine Maier, Cornelius Hempel, Petar Jurcevic, Ben P. Lanyon, Thomas Monz, Michael Brownnutt, Rainer Blatt, and Christian F. Roos. Electromagnetically-induced-transparency ground-state cooling of long ion strings. *Physical Review A*, 93(5):053401, May 2016. Publisher: American Physical Society. URL: https://link.aps.org/doi/10.1103/PhysRevA.93.053401, doi:10.1103/PhysRevA.93.053401.

[24] Jonathan Home. Quantum Optics. Lecture Notes, January 2021.

[25] Wikipedia. Gaussian beam, October 2022. Page Version ID: 1117302012. URL: https://en.wikipedia.org/w/index.php?title=Gaussian_beam&oldid=1117302012.

[26] Bahaa E. A. Saleh and Malvin Carl Teich. *Fundamentals of photonics*. Wiley series in pure and applied optics. Wiley, Hoboken, NJ, third edition edition, 2019.

[27] Léon Brillouin. Diffusion de la lumière et des rayons X par un corps transparent homogène - Influence de l'agitation thermique. *Annales de Physique*, 9(17):88–122, 1922. Number: 17 Publisher: EDP Sciences. URL: https://www.annphys.org/articles/anphys/abs/1922/17/anphys19220917p88/anphys19220917p88.html, doi:10.1051/anphys/192209170088.

[28] P. Debye and F. W. Sears. On the Scattering of Light by Supersonic Waves. *Proceedings of the National Academy of Sciences*, 18(6):409–414, June 1932. URL: https://pnas.org/doi/full/10.1073/pnas.18.6.409, doi:10.1073/pnas.18.6.409.

[29] E. A. Donley, T. P. Heavner, F. Levi, M. O. Tataw, and S. R. Jefferts. Double-pass acousto-optic modulator system. *Review of Scientific Instruments*, 76(6):063112, June 2005. URL: http://aip.scitation.org/doi/10.1063/1.1930095, doi:10.1063/1.1930095.

[30] AA optoelectronics. Application Notes. Technical report. URL: http://www.aaoptoelectronic.com/wp-content/uploads/documents/AA-THEORY-NOTES.pdf.

[31] AA Optoelectronic. DTSX - DTSXY. Datasheet, AA Opto-electronic, February 2007. URL: https://web.archive.org/web/20220518153852/http://www.aaoptoelectronic.com/wp-content/uploads/2018/08/DTSxx-ed1-18.pdf.

[32] AA Optoelectronic. MT350-A0.12-xx. Technical report, AA Opto-electronic, December 2006. URL: https://web.archive.org/web/20230227110304/http://www.aaoptoelectronic.com/wp-content/uploads/2018/08/MT350-A0.12-xx-ed2-18.pdf.

[33] Héctor Sainz Cruz. *Huygens-Fresnel diffraction of Hermite-Gaussian modes by a circular aperture*. semester thesis, ETH Zurich, June 2018. URL: https://web.archive.org/web/20230302120404/https://ethz.ch/content/dam/ethz/special-interest/phys/quantum-electronics/tiqi-dam/documents/semester_theses/semesterthesis_Hector_Sainz_Cruz.

[34] Martin Ringbauer, Michael Meth, Lukas Postler, Roman Stricker, Rainer Blatt, Philipp Schindler, and Thomas Monz. A universal qudit quantum processor with trapped ions. *Nature Physics*, 18(9):1053–1057, September 2022. Number: 9 Publisher: Nature Publishing Group. URL: https://www.nature.com/articles/s41567-022-01658-0, doi:10.1038/s41567-022-01658-0.

[35] Jouko Vankka and Kari Halonen. *Direct Digital Synthesizers*. Springer US, Boston, MA, 2001. URL: http://link.springer.com/10.1007/978-1-4757-3395-2, doi:10.1007/978-1-4757-3395-2.

[36] Thorlabs. Using the Poincare Sphere to Represent the Polarization State. URL: https://www.thorlabs.com/newgrouppage9.cfm?objectgroup_id=14200.

[37] Dave Jones. picamera — Picamera 1.13 Documentation. URL: https://picamera.readthedocs.io/en/release-1.13/.

[38] Raspberry Pi Ltd. Buy a Raspberry Pi Camera Module 2. URL: https://www.raspberrypi.com/products/camera-module-v2/.

[39] Sylvain de Léséleuc. *Quantum simulation of spin models with assembled arrays of Rydberg atoms*. PhD thesis, Université Paris-Saclay, December 2018. URL: https://oqatomlcfio.files.wordpress.com/2019/01/phd_thesis_deleseleuc_sylvain.pdf.

[40] Robert J. C. Spreeuw. Off-Axis Dipole Forces in Optical Tweezers by an Optical Analog of the Magnus Effect. *Physical Review Letters*, 125(23):233201, December 2020. Publisher: American Physical Society. URL: https://link.aps.org/doi/10.1103/PhysRevLett.125.233201, doi:10.1103/PhysRevLett.125.233201.

[41] Robert J. C. Spreeuw. Spiraling light: from donut modes to a Magnus effect analogy. *Nanophotonics*, 11(4):633–644, January 2022. Publisher: De Gruyter. URL: https://www.degruyter.com/document/doi/10.1515/nanoph-2021-0458/html, doi:10.1515/nanoph-2021-0458.

[42] M. Mazzanti, R. Gerritsma, R. J. C. Spreeuw, and A. Safavi-Naini. Trapped Ion Quantum Computing using Optical Tweezers and the Magnus Effect, January 2023. arXiv:2301.04668 [physics, physics:quant-ph]. URL: http://arxiv.org/abs/2301.04668.

[43] Joseph J M Braat, Peter Dirksen, and Sven van Haver. Detailed description of the ENZ approach, 2015. URL: https://nijboerzernike.nl/_PDF/NijboerZernike_webpage_detailed_20151023.pdf.

[44] Joseph Braat. Aberration retrieval using the extended Nijboer-Zernike approach. *Journal of Micro/Nanolithography, MEMS, and MOEMS*, 2(1):61, January 2003. URL: http://nanolithography.spiedigitallibrary.org/article.aspx?doi=10.1117/1.1531191, doi:10.1117/1.1531191.

[45] C. Van der Avoort, J. J. M. Braat, P. Dirksen, and A. J. E. M. Janssen. Aberration retrieval from the intensity point-spread function in the focal region using the extended Nijboer–Zernike approach. *Journal of Modern Optics*, 52(12):1695–1728, August 2005. doi:10.1080/09500340500072547.

[46] Augustus J. E. M. Janssen. Extended Nijboer–Zernike approach for the computation of optical point-spread functions. *Journal of the Optical Society of America A*, 19(5):849, May 2002. URL: https://opg.optica.org/abstract.cfm?URI=josaa-19-5-849, doi:10.1364/JOSAA.19.000849.

[47] Alfredo Ricci Vasquez, Carmelo Mordini, Chloé Vérnière, Martin Stadler, Maciej Malinowski, Chi Zhang, Daniel Kienzler, Karan K. Mehta, and Jonathan P. Home. Control of an atomic quadrupole transition in a phase-stable standing wave, October 2022. arXiv:2210.02597 [physics, physics:quant-ph]. URL: http://arxiv.org/abs/2210.02597, doi:10.48550/arXiv.2210.02597.

[48] Ali Binai-Motlagh, Matthew Day, Nikolay Videnov, Noah Greenberg, Crystal Senko, and Rajibul Islam. A guided light system for agile individual addressing of Ba$^+$ qubits with 10^{-4} level intensity crosstalk, February 2023. arXiv:2302.14711 [physics, physics:quant-ph]. URL: http://arxiv.org/abs/2302.14711.

[49] Marco Canteri. Single-atom-focused laser for photon generation and qubit control. Master's thesis, University of Innsbruck, 2020. URL: https://web.archive.org/web/20230224120911/https://quantumoptics.at/images/publications/diploma/master_Marco_Canteri.pdf.

[50] Tom Manovitz. Individual Addressing and Imaging of Ions in a Paul Trap. Master's thesis, Weizmann Institute of Science, March 2016. URL: https://web.archive.org/web/20230302105806/https://www.weizmann.ac.il/complex/ozeri/sites/complex.ozeri/files/uploads/thesis_submission.pdf.

[51] Lukas Pernthaler. Single Ion Addressing of up to 50 Ions. Master's thesis, Leopold-Franzens University of Innsbruck, August 2019. URL: https://web.archive.org/web/20221031011100/https://www.quantumoptics.at/images/publications/diploma/master_pernthaler_SingleIonAddressing.pdf.

[52] Andreas Pöschl. Laser Ablation Loading and Single Ion Addressing of Strontium in a Linear Paul Trap. Master's thesis, KTH Royal Institute of Technology, April 2018. URL: https://web.archive.org/web/20230302104714/https://kth.diva-portal.org/smash/get/diva2:1203307/FULLTEXT01.pdf.

Eidgenössische Technische Hochschule Zürich
Swiss Federal Institute of Technology Zurich

Declaration of originality

The signed declaration of originality is a component of every semester paper, Bachelor's thesis, Master's thesis and any other degree paper undertaken during the course of studies, including the respective electronic versions.

Lecturers may also require a declaration of originality for other written papers compiled for their courses.

I hereby confirm that I am the sole author of the written work here enclosed and that I have compiled it in my own words. Parts excepted are corrections of form and content by the supervisor.

Title of work (in block letters):

Single-ion addressing using crossed acousto-optic deflectors

Authored by (in block letters):

For papers written by groups the names of all authors are required.

Name(s):	First name(s):
Timme	Hendrik

With my signature I confirm that

- I have committed none of the forms of plagiarism described in the 'Citation etiquette' information sheet.
- I have documented all methods, data and processes truthfully.
- I have not manipulated any data.
- I have mentioned all persons who were significant facilitators of the work.

I am aware that the work may be screened electronically for plagiarism.

Place, date	Signature(s)
Zürich, 27.03.2023	

For papers written by groups the names of all authors are required. Their signatures collectively guarantee the entire content of the written paper.

A Settings of the camera

Listing A.1 shows the python code included before every capture of the camera to set fixed parameters to be able to compare measurements. We would like the camera to not apply any variable exposure or gain depending on the brightness of the image. This way we can set them manually.

```python
def setcameraparameters(camera):
    '''
    Parameters
    ----------------------------------------
    camera : call Picamera.camera class
    ----------------------------------------
    sets parameters for the camera class,
    so they are consistent between captures.
    '''
    camera.iso = 500
    sleep(2) # wait for the automatic gain control to settle

    # now fix the values
    camera.shutter_speed = 30000
    camera.exposure_mode = 'off'
    camera.awb_mode = 'off'
    camera.awb_gains = 1.4
    return
```

LISTING A.1: Code used in order to fix camera values.

To check whether the camera is saturating we looked at the brightest recorded pixel and increased the intensity of the laser beam. The result can be seen in figure A.1. Each point represents the average of 100 photos taken at the specified power. In order to speed up the process on the pi we used the `camera.zoom()` and `camera.resolution()` functions to restrict the area of capture. The images have been converted to grayscale.

To measure the intensity distributions of the laser beam, we have to convert pixel brightness to electric field intensity. We would like a linear relationship between the pixel intensity and the intensity of the beam. To achieve this we always took pictures in the regime where the brightest pixel had a brightness value of less than 100. We programmed a short script to read out the brightest pixel. We included a set of waveplates and a polarized beamsplitter in the beam path before the waveplates before the AOD. Before every measurement, we could then calibrate the waveplates in front of the polarized beam splitter, so that the camera is not oversaturated.

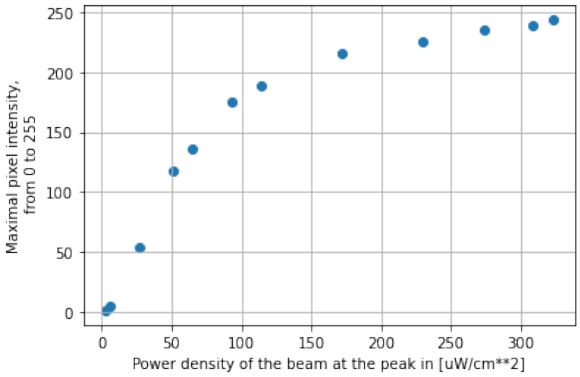

FIGURE A.1: Calibration measurement for the picamera v2.

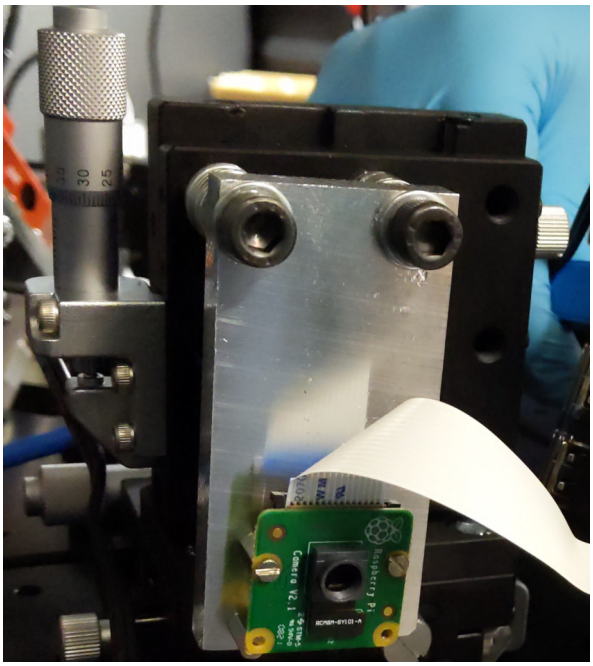

FIGURE A.2: Shown is the scrap piece of aluminum the camera was mounted to so that it can be screwed to an adjustable stage.

B Phase retrieval and simulation using the extended Nieboer-Zernike theory

To test the phase retrieval algorithm, we simulate data using a pre-determined set of aberration coefficients using equation 4.27. We then test the phase retrieval capabilities of the algorithm described in section 4.4. The simulated intensities can be seen in figures B.1a - B.1d. In table B.1 the chosen Zernike coefficients versus the retrieved Zernike coefficients are shown. Any parameter not listed is set to zero.

aberration	coefficient used to simulate	retrieved coefficient
spherical	$\alpha_{20} = 0, \alpha_{40} = 1$	$\alpha_{20} = -4.3 \cdot 10^{-6}, \alpha_{40} = 1.000$
coma	$\alpha_{11} = 0, \alpha_{31} = 1$	$\alpha_{20} = -6.7 \cdot 10^{-4}, \alpha_{40} = 1.006$
astigmatism	$\alpha_{22} = 1$	$\alpha_{22} = 1.001$

TABLE B.1: Excerpt of the test sheet supplied by opto-electronic for AOD DTSXZ-400-730-020.

The results show that the algorithm can retrieve aberrations with a precision of the order of 10^{-3}.

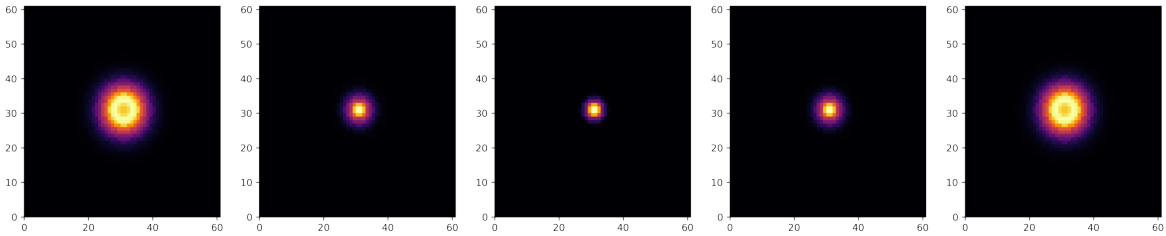

(A) Simulated intensities with no aberrations.

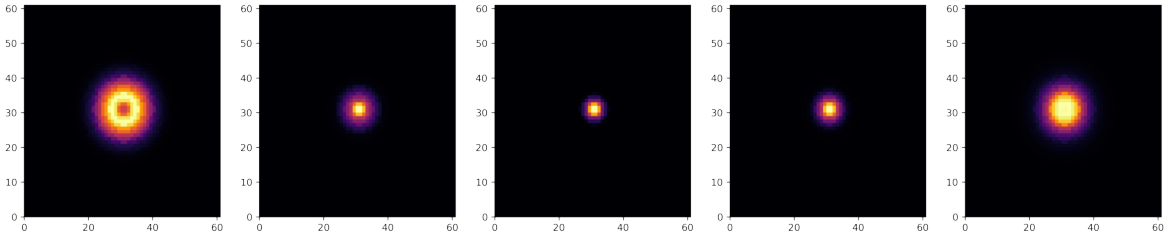

(B) Simulated intensities with spherical aberrations.

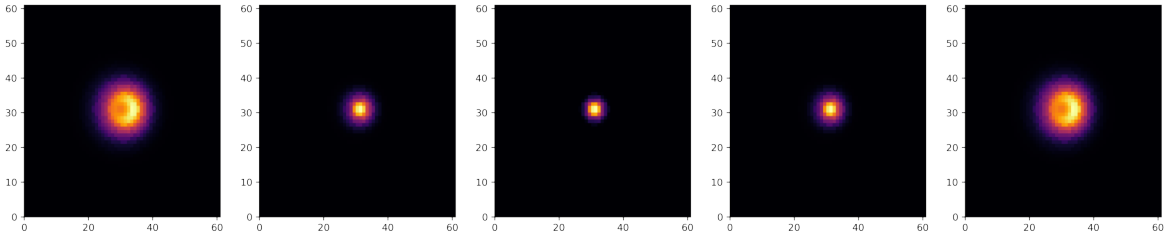

(C) Simulated intensities with coma

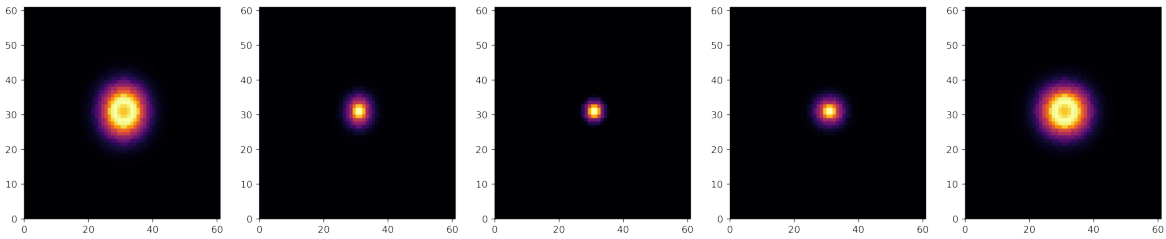

(D) Simulated intensities with astigmatism.

FIGURE B.1: Simulated Intensities to test retrieval capabilities. The defocus parameters chosen are $f = \{-2\pi + 2i, -1\pi + 2i, 2i, 1\pi + 2i, 2\pi + 2i\}$, so that the aberrations are visible in the simulated intensities.